

**Investigation of a differentially powered multi-tile VHF CCP using
particle in cell simulation**

Joachim Bosschaert, B.Sc


A thesis presented for the degree of
Master of Science

School of Physical Sciences
Dublin City University

August 2023

Supervisor: Dr. A.R. Ellingboe

I hereby certify that this material, which I now submit for assessment on the programme of study leading to the award of Master of Science is entirely my own work, and that I have exercised reasonable care to ensure that the work is original, and does not to the best of my knowledge breach any law of copyright, and has not been taken from the work of others save and to the extent that such work has been cited and acknowledged within the text of my work.

Signed:  ID No. 16461956 : Date: 16 June 2023

Joachim Bosschaert

Plasma Research Laboratory
School of Physical Sciences
Dublin City University
Dublin, Ireland

Acknowledgements

I'd like to thank Dr. Bert Ellingboe. Thanks to his guidance, teaching and patience I have been able to pursue this degree in Plasma physics.

To friends I've made throughout my postgraduate journey in DCU; Shane, Adam, Caitlin, Andrew and Orlaith. Thanks for keeping morale high. You have all deeply enriched my experience in DCU.

Thanks to Klaudia, and my parents, Winnie and David who have supported me through everything.

Contents

1	Introduction	2
1.1	Plasma Theory	2
1.1.1	What is plasma	2
1.1.2	Electron motion	3
1.1.3	Plasma Frequency	4
1.1.4	Plasma shielding and Debye length	5
1.1.5	Plasma Parameters	6
1.2	Sheath formation	7
1.3	Capacitively coupled plasma	8
1.4	Surface processing	10
1.4.1	Very high frequency domain	13
1.5	Differential power coupling	13
2	Fundamentals of plasma simulation	17
2.1	What are plasma simulations	17
2.2	Types of plasma simulation	17
2.3	Operation of a Particle in Cell code	19
2.4	Particle movement	20
2.5	Field Solvers	22
2.6	Stability criteria for electromagnetic PIC codes	24
3	Investigation of power coupling in a differentially powered multi-tile VHF CCP using particle in cell simulation	27
3.1	Introduction	27
3.2	Description of the model and plasma system	32
3.3	Power Coupling	36
3.3.1	Electromagnetic power coupling	36
3.3.2	Electrostatic power coupling	38
3.3.3	Plasma density	40
3.4	Currents and magnetic fields	41
3.5	Power coupling in the plasma	44
3.6	Plasma response at a differentially-powered tile-pair	47
3.6.1	Generalized Ohms law	47
3.6.2	Faraday's Law solution	52
4	Variation in plasma coupling with drive current	57
4.1	Introduction	57
4.2	Low current and high current experiments	57
4.3	Spatial density profile vs driving current	65
4.4	Difference between coupling and non-coupling region	66
4.5	Voltage profile on differentially powered tiles	70
4.6	Coupled current and substrate current scaling	73
4.7	Electromagnetic response in the higher current simulation	76
4.8	Summary	77

5 Conclusion	79
6 Appendix	82

List of Figures

1.1	Transition of potential from plasma bulk, to the sheath to the boundary of the plasma	8
1.2	Symmetric capacitively coupled plasma.	9
1.3	Plasma potential at different moments in the <i>rf</i> cycle	10
1.4	Typical CCP system that can perform surface processes on a wafer	11
1.5	Differential power coupling. (a) shows current moving across the plasma boundary as in a symmetric CCP. (b) shows the electric field due to a variation in plasma potential oscillation driving a current parallel to the face of the tiles. (c) shows the magnetic dipole between adjacent tiles, driving an induced electric field that brings current from one tile to the adjacent tile. [1]	14
2.1	Computational cycle for a particle in cell program	20
3.1	3 geometric configurations of CCP coupling. a) shows a symmetric CCP with two electrodes of equal area. b) shows an asymmetric CCP, where one electrode has a larger area than the other. c) shows a seemingly symmetric CCP (powered to un-powered area) but where one electrode is split into two differentially powered tiles.	28
3.2	Simulated plasma chamber, analysed area in the blue dotted rectangle. Tiles labelled 1-6, and will be referred to as such.	34
3.3	(a) Magnetic fields generated by currents on the surface of electrodes, induced electric field due to time varying magnetic field. Red arrows show currents travelling on the surface of the tile. (b) Current coupled from one tile to adjacent tile due to the induced electric field created by the magnetic field between the tiles. The orange arrows represent the current path due to the induced EMF created by the changing magnetic field.	37

3.4	Contour plot of electron density in the plasma volume at two moments in the <i>rf</i> cycle; a) Voltage on tile 3 is at a maximum, b) voltage on tile 4 is at a maximum. A very small change in density ($\approx 1\%$) in plasma in front of adjacent tiles is observed over the <i>rf</i> cycle.	40
3.5	<i>rf</i> current in (a) the \hat{x} direction, (b) the \hat{y} direction, and (c) magnetic field in \hat{z} direction between the two central tiles at the same point in time.	42
3.6	Current path in simulation at three different phases. Figure 3.6(a) is when current into the tiles is maximal at 0 degree phase (<i>Tile</i> ₃ powered with current waveform $I(t) = I_0 \sin(\omega t + \phi)$). Figure 3.6(c) shows current at 90 degree phase, when there is no coupled current between adjacent tiles. Figure 3.6(b) shows the transition between these two phases (45 degrees)	43
3.7	a) tile voltage and driving current over an <i>rf</i> cycle, b) coupled current, horizontal electric field and induced electric field over and <i>rf</i> cycle	45
3.8	Result of a fourier transform of horizontal electric field, showing relative amplitude of frequencies.	46
3.9	Terms from Generalized Ohms law plotted. The red curve shows the combination of the $\frac{dJ}{dt} + \nu_c J$, and the blue curve plots $\epsilon_0 \omega_{pe}^2 E$. The curves are almost equal, showing the model is a good fit. . .	50
3.10	Analytical model current densities compared to self-consistent Xoopic currents.(a) J_x from the analytical model, (b) J_x from Xoopic simulation,(c) J_y from the analytical model, (d) J_y from Xoopic simulation driven at 75A/m.	52
3.11	Y profile of currents in analytical model vs Xoopic simulation. . .	53

3.12	Path where Faraday’s Law is solved, with enclosed magnetic field.	54
3.13	(a) Electric Field in the x direction, (b) electric field in the y direction and (c) Time derivative of the enclosed magnetic field ($\omega B \cdot da$).	55
4.1	2D profiles across the center 4 tiles for a simulation driven at 50A. Current in (a) x-direction, (b) y-direction, (c) Magnetic field in z-direction and (d) electron density. Currents and magnetic fields are defined as the total current or magnetic field in that particular cell.	58
4.2	2D profiles across the center 4 tiles for a simulation driven at 150A. Current in (a) x-direction, (b) y-direction, (c) Magnetic field in z-direction and (d) electron density. Currents and magnetic fields are defined as the total current or magnetic field in that particular cell.	61
4.3	Conductive current vector in the plasma for lower current simulation (a), and higher current simulation (b).	63
4.4	Plasma density in the \hat{y} -direction for all values of driving current.	65
4.5	Plasma density in coupling region (red), non-coupling region (blue) and total plasma volume (grey)	67
4.6	Ionization rate vs y-position, for (a) 50A driving current, (b) 150A driving current.	68
4.7	Velocity distribution in the coupling region (red), and non-coupling region (blue) for Simulation driven at 50A (a) and simulation driven at 150A (b). Threshold for single step Argon ionization in Xoopic is 15.76eV, equating to a velocity of 2.35×10^6 m/s shown on the x-axis.	69

4.8	Tile voltage over and rf cycle (a), Amplitude of tile voltage(b), DC bias on tile (c)	71
4.9	Plasma current in the \hat{y} -direction with two bounding boxes used to calculate total coupled current and total current into the sub- strate.	74
4.10	Coupled current (a), and current into the substrate (b) as a func- tion of driving current.	75
4.11	Fraction of total current turned into coupled current (orange), fraction of total current that moves towards the substrate (brown)	76
4.12	Current in the y-direction from the Generalized Ohm's Law model (a) compared to current in the y-direction from Xoopic	77
6.1	A single powered tile in the 2D array of differentially powered tiles, Showing method of current injection into the tile via a Xoopic "current region". Self-consistent electric field between the tile and grounded boundary is shown, and is used to calcu- late the time-varying rf voltage on the powered tile.	83

Abstract

The Thesis titled: "Investigation of a differentially powered multi-tile VHF CCP using particle in cell simulation", is submitted by Joachim Bosschaert. A differentially powered, very high frequency (VHF), multi-tile, capacitively coupled plasma system is modelled using particle in cell simulation code, Xoopic [2]. The powered electrode in this system is split into an array of differentially powered tile. The current path is observed in the plasma; one pathway is towards the opposite grounded boundary; a second pathway is observed coupling between adjacent out-of-phase tiles (coupled current). Two physical phenomena are described that could drive the coupled current; An electrostatic phenomenon, due to a spatio-temporal variation in the plasma potential. And an electromagnetic phenomenon, due to a time-varying magnetic dipole between adjacent tiles that induces an electric field. Through solving Generalized Ohm's Law in the plasma system, and calculating the magnitude of the induced electric field, it is determined that the electrostatic mechanism is the dominant mechanism for driving the coupled current.

A region of higher plasma density is identified in front of the powered electrode. This region also supports a higher electron temperature and ionization rate. Most of the current in this region points from one electrode to the adjacent electrode. Towards the grounded electrode plasma density, electron temperature and ionization rate are lower and most of the current points towards the substrate. As driving current is increases, a larger fraction of driving current moves towards the adjacent tile rather than towards the grounded electrode.

1 Introduction

1.1 Plasma Theory

1.1.1 What is plasma

Plasma is a state of matter that consists of electrons, ions and neutral particles. It is often described as a quasi-neutral state as there are (almost) the same amount of electrons and ions. It is the presence of electrons and ions that make plasma a different state of matter to a gas. Electrons and ions are charged particles, which means that they can respond to electric and magnetic fields. This means that plasmas can be affected in very specific ways by adding external electric or magnetic fields. In a gas, there are few electrons and ions which respond to these fields. When the electron density and ion density is large enough, a new 'collective motion' of occurs which is fundamentally different to the behaviour of a gas.

The degree of ionization is an important aspect of the plasma, as it determines the ratio of ions (and electrons) to neutral gas particles.

$$\eta = \frac{n_i}{n_n + n_i} \quad (1.1)$$

Different plasmas have different degrees of ionization. Glow discharge capacitively coupled plasmas exhibit a low degree of ionization, ($10^{-3} - 10^{-6}$), meaning that the dominant interactions for the charged species occur between electrons and neutral particle collisions or between ions and neutrals. These collisions can be elastic or inelastic. If an electron has enough energy, a collision with a neutral can cause ionization. The sun is a plasma which has a much higher degree of ionization ($\eta \approx 1$), which means that almost all of the gas is ionized. Collisions in this plasma are almost all between charged particles. Meaning that most interactions are Coulomb collisions through the Coulomb force $F = k \frac{Q_1 Q_2}{r^2}$. The

rest of the thesis will concern only low ionization plasmas ($\eta < 0.001$), and more specifically what is called a non equilibrium low temperature plasma.

There are certain important parameters that must be considered when describing a plasma. One of these parameters is the plasma frequency, ω_{pe} (see section 1.1.3). This describes the response time of electrons in the plasma. In a plasma, the coulomb interaction between the charges means that the charges want to be arranged in a way that neutralizes all charge imbalance. This results in external electric and magnetic fields are shielded out by the electrons and ions over a certain scale length, the Debye length λ_D (section 1.1.4).

1.1.2 Electron motion

In a plasma, the electrons have different velocities. for electrons in a 3 dimensional equilibrium plasma, the electron velocity follows a Maxwell-Boltzmann distribution (equation 1.2).

$$f(v) = \left(\frac{m_e}{2\pi k_B T_e} \right)^{\frac{3}{2}} 4\pi v^2 e^{\left(\frac{-mv^2}{2k_B T_e} \right)} \quad (1.2)$$

This function describes the Thermal distribution of electrons in the plasma, with characteristic electron temperature T_e . The electron temperature can be used to describe the kinetic energy of electrons moving due to thermal energy in the plasma. At thermal equilibrium, in a plasma with plasma potential ϕ , electrons adopt a Boltzmann density distribution:

$$n_e = n_0 \exp\left(\frac{e\phi}{k_b T_e} \right) \quad (1.3)$$

where ϕ is the potential difference between the locations of n_e and n_0 . Every electron in the plasma has potential energy $-e\phi$ and thermal kinetic energy $k_B T_e$.

1.1.3 Plasma Frequency

If an electric field is applied to a plasma, the electrons will reposition themselves so that the Coulomb force between the electrons and ions balances the force experienced by the electric field. It is the electrons doing the movement and not the ions, because the electrons are light compared to the ions ($m_i : m_e = 1836 : 1$ for hydrogen, and for argon $m_i : m_e \approx 70,000 : 1$), due to their small moment of inertia, they are able to respond to the applied electric field much faster than the ions. In one dimension, Poisson's equation can be written as shown in equation 1.4. After integrating, the electric field can be expressed in terms of the charge density and the distance the charges are displaced (equation 1.5).

$$\frac{\partial E}{\partial x} = \frac{-en_e}{\epsilon_0} \quad (1.4)$$

$$E = \frac{-en_e}{\epsilon_0} dx \quad (1.5)$$

dx is the distance the electrons have moved from their original, previously electrically balanced position. The force applied to the particles is proportional to the electric field ($F = eE$), and this relationship can be used to set up the following differential equation 1.6.

$$E = \frac{\partial^2 x}{dt^2} + \frac{e^2 n_e}{m_e \epsilon_0} x = 0 \quad (1.6)$$

This equation describes a harmonic oscillator, where the characteristic frequency $\omega = \sqrt{\frac{e^2 n_e}{m_e \epsilon_0}}$. This characteristic frequency is the plasma frequency, and it defines the fastest response time of the plasma.

1.1.4 Plasma shielding and Debye length

Assume an infinite plasma, and a grid that is held at $\phi(x) = \phi_g$ is placed in this plasma. Electrons quickly react (time scale of $\tau \approx 1/\omega_{pe}$) to this change in potential and rearrange themselves so that the Coulomb force between the applied potential is balanced by the Coulomb force of other charged particles in the plasma. Beginning with the one dimensional Poisson equation (in terms of potential this time).

$$\frac{d^2\phi(x)}{dx^2} = \frac{-e(n_i - n_e)}{\epsilon_0} \quad (1.7)$$

Assuming that the ions are unperturbed, and the electrons are distributed according to a Maxwell-Boltzmann distribution, the following can be substituted into the equation.

$$\frac{d^2\phi(x)}{dx^2} = \frac{en_0}{\epsilon_0} \left[\exp\left(\frac{e\phi}{k_b T_e}\right) - 1 \right] \quad (1.8)$$

For a small potential perturbation, $\frac{e\phi(x)}{k_b T_e} \ll 1$, a Taylor expansion can be applied: $\exp\left(\frac{e\phi}{k_b T_e}\right) = 1 + \frac{e\phi}{k_b T_e}$. This results in the following differential equation.

$$\frac{d^2\phi}{dx^2} = \frac{e^2 n_0}{\epsilon_0 T_e} \phi \quad (1.9)$$

This equation has the following solution.

$$\phi(x) = \phi_0 \exp\left(-\frac{|x|}{\lambda_D}\right) \quad (1.10)$$

This equation describes a potential that decays exponentially with characteristic decay length of the Debye length, λ_D .

$$\lambda_D = \sqrt{\frac{\epsilon_0 T_e}{e^2 n_0}} \quad (1.11)$$

When a plasma receives a perturbation in potential, this perturbation does not extend into the plasma further than a few Debye lengths, λ_D . The Debye length is often described as the scale length of the plasma; There can be local variations in the plasma potential at length scales the order of λ_D , but at longer scale lengths these variations in plasma potential cannot exist due to the collective behaviour of the plasma electrons.

1.1.5 Plasma Parameters

In order for a substance to be considered a plasma, it must satisfy 3 criteria. The first criterion is that each particle must be close enough to many other particles that they interact through their electrostatic forces.

$$N_d = n \frac{4}{3} \pi \lambda_D^3 \gg 1 \quad (1.12)$$

N_d is known as the plasma parameter. This criterion is satisfied when the plasma parameter is much greater than 1, or in other words, when there are many particles within a sphere of radius λ_D .

The scale of the plasma must be much larger than the Debye length. The second criterion is that the Debye length $l \gg \lambda_D$. If this is satisfied, then the interactions in the bulk of the plasma are more important than the interactions at the boundary of the plasma. If this is not satisfied, then Debye shielding cannot occur in the plasma.

The third is that the plasma frequency must be greater than the collision frequency, $\omega_{pe} > \nu_c$. When this condition is violated, plasma response to an external force is dominated by collisional behaviour, akin to a gas, and not the collective behaviour of the plasma. The plasma can not shield out variations in potential, because (on average) the electrons collide with neutrals in a timescale

faster than they can react to changes in the local potential.

1.2 Sheath formation

On the boundary of a plasma, where the plasma is in contact with the wall a sheath region is formed. This is a region where there are fewer electrons and ions. In this region, the plasma is no longer quasi-neutral, which leads to a voltage drop in this sheath region between the plasma and the wall.

Consider a quasi-neutral plasma in contact with a wall. The wall acts like a sink for charges, so when an electron or ion comes in contact with the wall it is 'lost'. Due to electrons being much more mobile than ions, the electron flux towards the wall is much greater than the ion flux into the wall ($\Gamma_e \gg \Gamma_i$). After time $t \approx \frac{\lambda_D}{v_{th}}$ the electrons moving towards the wall are absorbed but the ions are nearly fixed in place due to the high mass and low temperature. This results in a region at the wall where there are fewer electrons than ions resulting in a net positive charge. In order for the plasma to reach a steady state, a condition must be found where the flux of electrons into the wall is balanced by the flux of ions into the wall ($\Gamma_e = \Gamma_i$), otherwise there would be a net loss of charge from the plasma.

According to Poisson's equation (equation 1.7), this positively charged region results in a change in the plasma potential. A sample sheath potential is shown in figure 1.1. The plasma "self-assembles" a charge distribution in the sheath, "shielding" the effects of the wall from the bulk plasma.

Due to this potential, ions are accelerated from the bulk plasma into the wall. This potential difference contains electrons within the plasma, reflecting most electrons that reach the sheath. Only electrons with thermal energy $k_B T_e > e\phi_s$ (where ϕ_s is the potential drop in the sheath or potential difference between the

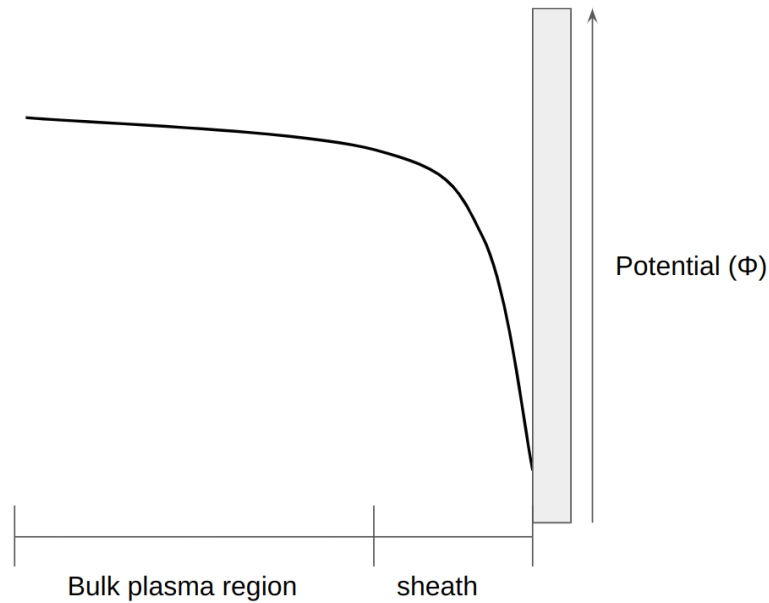


Figure 1.1: Transition of potential from plasma bulk, to the sheath to the boundary of the plasma

wall and the plasma) can overcome this potential and reach the sheath. In an equilibrium plasma, this results in a state where electron flux and ion flux into the wall are equal (in an *rf* plasma these fluxes would be equal over an *rf* cycle).

1.3 Capacitively coupled plasma

In a laboratory setting, a capacitively coupled plasma (CCP) is often used to create a plasma. A capacitively coupled plasma is comprised of two powered electrodes, with gas between the electrodes (shown in figure 1.2). energy is added to the plasma through a external electric and magnetic fields. Once the voltage on the electrodes reaches a certain point, the gas between the electrodes "breaks down" and a plasma is formed.

Industrial CCPs are often driven by a radio frequency (*rf*) AC current source

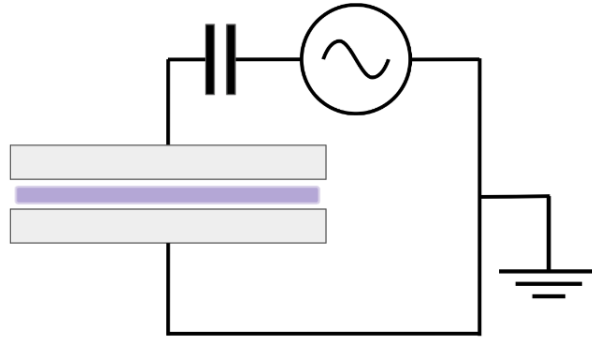


Figure 1.2: Symmetric capacitively coupled plasma.

(often 13.56MHz). Voltage on the electrodes are oscillating at radio frequency. The plasma sheaths also oscillate at this frequency. The plasma is in a regime where the ions are too slow to respond instantaneously to changes in fields at the driving frequency, and they respond to the time-averaged electric and magnetic fields. Electrons in the plasma move fast enough that they can respond to these changing fields ($\omega_{pe} > \omega \gg \omega_{pi}$). One consequence of this, is that a plasma can be struck at much lower voltages. In a DC plasma, a potential difference on the order of kiloVolts is often required to create a CCP, but in *rf* plasmas, this often on the order of tens to hundreds of volts (depending on the system used and type of gas used).

In a symmetric plasma source, as seen in figure 1.2, there are two electrode of equal area powering the plasma. Both electrodes have a time varying sheath, which varies with the *rf* voltage. When the sheath at one electrode expands, the sheath on the opposite side of the plasma contracts. Current that flows into one electrode, must flow through the plasma towards the opposite electrode.

In an asymmetric plasma source, where one electrode is larger than the other, a plasma potential oscillation can be observed. When a powered electrode

reaches its maximum voltage over the *rf* cycle, it slightly raises the plasma potential in front of that tile. When the tile reaches a minimum in voltage, it slightly lowers the potential in front of the tile. This results in an oscillation in the plasma potential. This oscillation is on the order of the electron temperature (T_e) [3]. For the plasma to be in steady state, same number of electrons and ions must strike the wall over an *rf* cycle. Therefore, there is a moment in time where $V_p - V_{electrode} < V_f$, allowing for a period of electron collection. The voltage over the *rf* cycle is shown in figure 1.3.

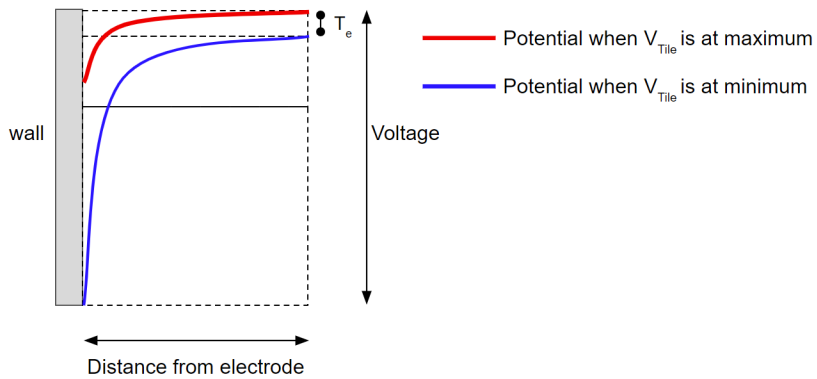


Figure 1.3: Plasma potential at different moments in the *rf* cycle

1.4 Surface processing

Processing surfaces on the microscopic level through using plasmas has become increasingly important in recent years. Surface processing is used in creating semiconductors which are used to make computers, it is used for patterning glass used in solar panels, it's used in manufacturing medical devices and many more applications. Many surface processes, such as plasma enhanced atomic layer deposition (PEALD), plasma enhanced atomic layer etching (ALE) involve a plasma source. Capacitively coupled plasma (CCP) reactors are often used in

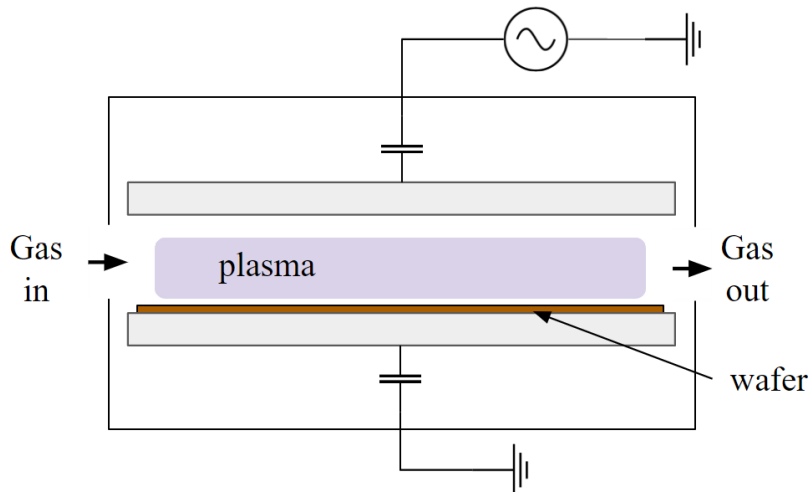


Figure 1.4: Typical CCP system that can perform surface processes on a wafer industry for surface processes.

In industry, CCPs are often used for various surface processes. A wafer is placed on one of the electrodes, and interactions between the plasma and this wafer can change the surface of the wafer on a microscopic level. Figure 1.4 shows such a plasma system. Ions and reactive species in the plasma move in the sheath towards the substrate where they interact or are deposited on the surface. Important parameters for surface processing are plasma density, ion flux, ion energy and plasma chemistry.

Control of ion energy is a crucial factor in surface processing. When an ion strikes a surface, a number of things can happen. If the ion energy is high, ion impact on the substrate can directly eject atoms from the surface via momentum transfer and particle recoil [4]. This is known as sputtering. In some processes this is desirable; for example in reactive ion etching, material is removed from the substrate in a specific pattern via ion sputtering. In other processes this

can be undesirable as this can cause unwanted damage to the substrate. At lower energies, the ions can "activate" the surface. When an ion collides with the surface the ion deposits its energy into molecules or atoms on the top layer of the surface. These atoms or molecules more easily react with reactive species in the plasma. This is a process that is often used in atomic layer etching, to remove layers from the substrate, or in atomic layer deposition to more easily deposit material on the substrate. If the ion energy is too low, the surface will not become "activated" and interactions between reactive species in the plasma and the surface material will not occur [5].

Using an *rf*CCP, ion energy can be controlled. The ions have low velocity in the bulk, but when they reach the sheath they gain energy. This means that the potential difference between the bulk plasma and the wall determines the energy at which ions reach the substrate. When driving the electrodes, due to the fast motion of electrons, the electrode receives a negative bias. Part of this DC bias is called the *rf*self bias and scales with the amplitude of the *rf*voltage on the electrodes, and with the driving frequency. There are numerous ways to control the ion energy [6, 7]. Sharma et al [8] have shown control through changing the driving frequency and *rf*Voltage. This varies the plasma potential and ultimately aids in tailoring the ion energy distribution into the grounded wall.

Ion flux into the substrate and plasma density are important parameters as they determine how many electrons reach the substrate to create an interaction. The ion flux in itself is the rate of ions reaching the substrate. The plasma density plays a role in determining the ion flux; If the sheath is collisionless, then the ion flux into the substrate is the number of ions leaving the bulk plasma,

going into the sheath and reaching the substrate. This can be controlled using an *rf* plasma. Sharma et al have [8] shown that plasma density can be controlled by varying the RF driving voltage and the driving frequency. The number of electron-neutral collisions causing ionization, and subsequently plasma density both increase by increasing the driving frequency [9].

1.4.1 Very high frequency domain

Typically, *rf* plasmas are driven by a waveform oscillating at $f = 13.56\text{MHz}$. This frequency was allocated for industrial application so it does not interfere with communications. It has been shown that increasing the *rf* frequency into the very high frequency (VHF) band (30MHz - 300MHz) is beneficial for certain plasma processes[9].

Through particle in cell (PIC) simulation, it has been shown that plasma density can be increased by increasing the driving frequency [10]. Vahedi et. al have also shown through PIC simulation that increasing the driving frequency results in a higher plasma density, and have also shown a lower plasma potential and smaller sheath width, which leads to a lower ion energy into the wall [11]. Moreover it has been shown that in a plasma enhanced chemical vapour deposition system, the deposition rate increased by up to a factor of 4 when driving frequency was changed from 30MHz to 115MHz, without causing ion induced damage [12].

1.5 Differential power coupling

The focus of this thesis is the modelling of a multi-tile differentially powered VHF CCP. This CCP is similar to a classic CCP, except one of the electrodes is split into a 2D array of differentially powered tiles (shown in figure 1.5). While

one tile is at a maximum in voltage, the adjacent tile is at a minimum in voltage. This results in a current path that moves parallel to the face of the tiles, joining plasma current that is moving away from one sheath with plasma current that moves towards the sheath at the adjacent tile. We define this current as the "coupled current".

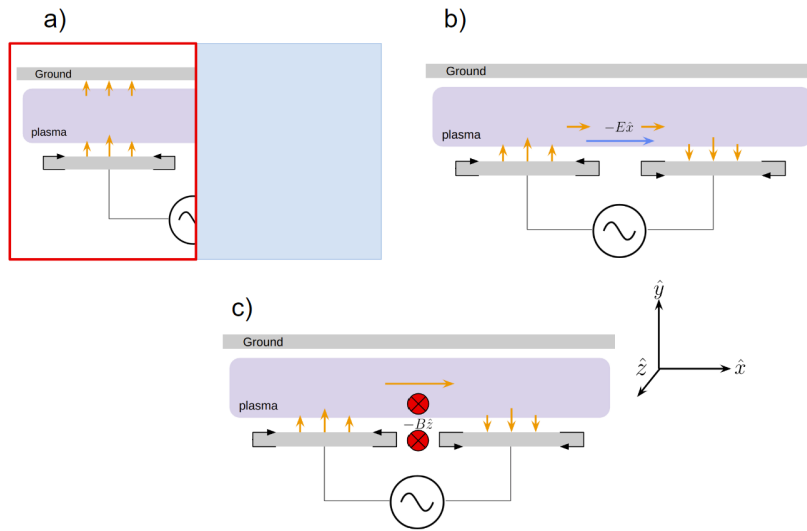


Figure 1.5: Differential power coupling. (a) shows current moving across the plasma boundary as in a symmetric CCP. (b) shows the electric field due to a variation in plasma potential oscillation driving a current parallel to the face of the tiles. (c) shows the magnetic dipole between adjacent tiles, driving an induced electric field that brings current from one tile to the adjacent tile. [1]

Tiles are differentially powered, such that current going into the left tile is $I = I_0 \sin(\omega t)$ and current into the adjacent tile is driven by $I = I_0 \sin(\omega t + \pi)$. Discussed previously, the *rf* current drives a plasma potential oscillation in the plasma in front of the tiles. The plasma potential in front of the left tile is oscillating 180 degrees out of phase with the plasma potential in front of the adjacent tile, driving an electric field in the plasma parallel to the tiles. This electric field drives some of the coupled current.

There is also an electromagnetic phenomenon driving the coupled current; Observing figure 1.5 (c), While current is pushed into the back of the left tile, current is pulled out of the back of the right tile. The *rf*Current travels on the surface of the tiles, creating magnetic fields oscillating at the same frequency. At the depicted moment in time, current travels into the left tile. On the right side of the left tile (at the tile-plasma interface), the current on the tile creates a magnetic field in the $-\hat{z}$ -direction. This magnetic field is created between the tile-tile gap and in the chamber just above this portion of the tile. On the right tile, a magnetic field is created on the left side of the tile (again at the tile-plasma interface). This magnetic field is also in the $-\hat{z}$ -direction, in phase with the magnetic field created by the other tile. This results in a time-varying magnetic dipole in the tile-tile gap, extending into the plasma volume. By Faraday's law ($\nabla \times E = -\frac{\partial B}{\partial t}$), this magnetic field creates an induced electric field that drives current in a loop around this magnetic dipole. In the plasma region above the tile-tile gap, the induced electric field points horizontally, parallel to the face of the tiles. This means that current moving away from one tile experiences this horizontal electric field, moves parallel to the face of the tiles and joins the current moving towards the adjacent tile.

Some of the current moving away from the tile becomes "coupled current" and joins with current moving towards the adjacent tile. This means that current density on the powered electrode does not equal the current density on the unpowered electrode. A high plasma density, and a high ion flux can be achieved without having a high *rf*current density at the unpowered electrode (where surface interactions would take place). Low *rf*current density at the unpowered results in a low sheath voltage and hence a low ion bombardment energy at the unpowered electrode. This results in a system that can achieve

high ion flux, and high plasma density while maintaining a low ion energy at the substrate.

The dynamics of this system of been postulated in various publications [13, 1, 14], but have never been fully understood. First, in chapter 3 we develop and understand the physics of this *rf*CCP. In chapter 4 we show how the plasma scales with increasing the amplitude of the driving current.

2 Fundamentals of plasma simulation

2.1 What are plasma simulations

Plasma simulations are computer-based models that are used to study the behaviour of plasmas. Due to the complex nature of plasmas, it is often difficult to understand what is happening in the plasma at a fundamental level. Plasma simulations allow researchers to study the behaviour of plasmas under a wide range of conditions, such as different temperatures, densities, and magnetic field strengths, without conducting any physical experiment. This allows researchers to gain insight into various useful diagnostics, such as electron temperature (T_e), the electron energy distribution function (EEDF), time-varying electric and magnetic fields, plasma currents and many more.

There are many different types of plasma simulations, and the specific methods used depend on the problem being studied and the level of detail required. Some common methods for simulating plasmas include particle-in-cell (PIC) simulations, fluid simulations, and hybrid simulations that combine both PIC and fluid approaches.

Plasma simulations are often used in conjunction with other tools and techniques, such as analytical models, experiments, and observations, to better understand the behaviour of plasmas in different environments. They are an important tool for researchers in fields such as astrophysics, materials science, chemical engineering, and fusion energy research, among others.

2.2 Types of plasma simulation

In fluid simulations, the plasma behaves as a fluid in a magnetic field acted on by a Lorentz force [15]. There is no notion of individual particles; electrons and ions are seen as fluids that respond to electric and magnetic fields. This

approach implicitly assumes that the plasma is collisional with particles having Maxwellian distributions. The time scale of these simulations is on the order of the electron ion collision frequency.

In Hybrid simulations, electrons are still seen as fluids, but ions are seen as particles that respond to electromagnetic forces [16]. This allows researchers to study the behaviour of ions at smaller time scales (up to the ion cyclotron frequency) and shows more accurate modelling of the ions as no assumptions are made about the ion distribution. The ion distribution function has dimensions (3 velocity and 3 position) and many ions must be simulated to get an accurate representation of their dynamics, this means that more computational power is required to simulate hybrid models than fluid models.

In “particle in cell” (PIC) models, the simulation volume is mapped onto a grid. For every gridcell there exists some electric and magnetic field. Electrons and ions are both considered to be particles which experience the forces in their given grid cells. Electrons move much faster than ions, meaning that the time-step for the evolution of these simulations must be much smaller to adequately resolve the electron motion; The electron plasma frequency (ω_{pe}) is the fastest response time for a PIC simulation and must be resolved. A large number of electrons and ions must be simulated in order to get an accurate representation of their distribution. In 3 dimensional PIC codes, ions and electrons have a 6 dimensional distribution function (3 velocity and 3 position). The smaller timescale of the simulation along with simulating millions of particles makes PIC the most computationally expensive of the three methods discussed. PIC simulations include the full kinetics of individual electrons and ions in motion and thus can simulate the behaviour of the plasma much more accurately; The resolution of electron motion allows such codes to simulate dynamics of *rf*sheaths, and various other effects occurring at the *rf*time scale.

In this thesis, PIC simulations have been conducted. The plasma that is being simulated has a driving frequency of 160MHz. Historically in *rf*CCPs electron transport through the sheath are not solved accurately by fluid or hybrid codes. Due to this there is a need to simulate this plasma system using PIC simulations.

2.3 Operation of a Particle in Cell code

In PIC simulations, a model of the plasma is created by simulating electron and ion behaviour when acted on by electric and magnetic fields. The velocities and positions of electrons are updated through Newton's equations of motion. Electric and magnetic fields are both applied externally and calculated from charge and current densities in the plasma.

PIC simulations are an iterative process (Figure 2.1). A computational cycle is defined, and then repeated for a set amount of timesteps. The locations all boundaries, regions and source in the simulation are defined, and a grid is imposed over these boundaries. The intersections of the grid are nodes and the squares (cubes in 3D) between gridlines are cells. Particles are described by their position and velocity coordinates. The particles can be collected and averaged such that a charge density and current is known at cells in the grid. In this way current density and charge density can be stored in a matrix of dimensions: [number of cells in x direction, number of cells in the y direction]. Electric field and magnetic field at all gridcells are calculated using a field solver (see section 2.5). With the field solver, the current density, charge density and previous electric and magnetic fields in adjacent locations on the grid are used to solve a set of equations to calculate a new set of electric and magnetic fields at this location. After this, at each cell the force is calculated using the Lorentz Force $F = q \cdot (E + v \times B)$. The particles experience the force at the cell in

which they are calculated, or a weighted average of forces from adjacent cells. Particles are accelerated in the direction of the force. Then equations of motion (Section 2.4) are used to give the particles new positions and velocities. This process is called the computational cycle, and is completed millions of times to reach a state where the plasma simulation yields a result.

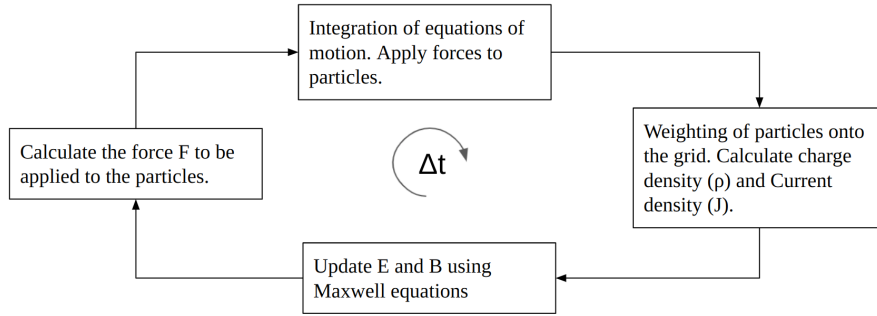


Figure 2.1: Computational cycle for a particle in cell program

The code used in this Thesis is Xoopic [2]. Xoopic is a fully kinetic particle in cell code with 2 spatial degrees of freedom and 3 degrees of freedom in velocity space.

2.4 Particle movement

In Xoopic [2] particles are updated according to the leapfrog method. The leapfrog method is a way to update particle position and velocity asynchronously in order to achieve a more stable simulation. Leapfrog method is used in many plasma simulations, as it requires very little memory, and has vanishing error as Δt approaches 0. Forces and positions are calculated at integer multiples of the timestep, while velocities are calculated at half integer timesteps. The equations of motion are as follows:

$$m \frac{dv}{dt} = F \quad (2.1)$$

$$\frac{dx}{dt} = v \quad (2.2)$$

To solve these equations, a number of different numerical methods can be used. In Xoopic, finite difference methods for the equations of motion are used. In the 1st equation of motion (Newton's 2nd Law), $\frac{dv}{dt}$ is approximated by taking the change in velocity as the difference in velocity at two half integer timesteps, and dividing by the time between these two measurements.

$$m \frac{v_{t+\frac{1}{2}\Delta t} - v_{t-\frac{1}{2}\Delta t}}{\Delta t} = F_t \quad (2.3)$$

At time t , we know the force (Calculated from field solver, (see section 2.5)) and the velocity at time $t - \frac{1}{2}\Delta t$, $v_{t-\frac{1}{2}\Delta t}$ is known. This equation can be rearranged to calculate $v_{t+\frac{1}{2}\Delta t}$. When $v_{t+\frac{1}{2}\Delta t}$ is known, the position of the particle can be updated. This is done by using the basic knowledge that velocity is the rate of change of time with respect to position $v = \frac{dx}{dt}$.

$$\frac{x_{t+\Delta t} - x_t}{\Delta t} = v \quad (2.4)$$

The velocity is assumed to be the constant value of $v_{t+\frac{1}{2}\Delta t}$ between t and Δt . At time $t + \frac{1}{2}\Delta t$, the velocity at x_t and $v_{t+\frac{1}{2}\Delta t}$ are known, and can be used to calculate $x_{t+\Delta t}$. The positions and velocities of particles have been updated, and are weighted to points on the grid to calculate current densities and charge densities. These current and charge densities are used to calculate a new set of electric and magnetic fields (which are then used as input for the particle mover at the next timestep).

At the beginning of the simulation, to allow for temporal offset between position and velocity, Force is calculated at $t=0$. This is used to calculate

velocity at $t = -\frac{1}{2}\Delta t$.

The number of particles in a CCP is often between 10^{14} and 10^{18} . Simulating this many particles takes a lot of computational power, as all particles need to be pushed individually at every timestep. In PIC simulations, a superparticle is defined, which is a single particle with the mass and charge of many individual particles. This superparticle acts as many particles in the same place at the same time. Superparticles are often defined to have the mass and charge of tens of millions to hundreds of millions individual particles, thus reducing the compute time by a factor of tens of millions.

2.5 Field Solvers

In PIC simulations of plasmas generally there are 2 solvers used; An electrostatic solver and an electromagnetic solver. In an electrostatic solver, the Poisson equation (equation 2.5) is solved computationally at every point in the simulation. Poisson's equation calculates an electric potential at every gridcell in the simulation, and pushes particles according to the electric field created by this potential ($E = \nabla\phi$). Electrostatic solvers do not consider the electromagnetic fields, thus they are useful when there are static magnetic fields, or when electric and magnetic fields are changing very slowly.

$$\nabla^2\Phi = \frac{\rho}{\epsilon} \tag{2.5}$$

In electromagnetic solvers, Ampere's law (equation 2.6) and Faraday's Law (equation 2.7) are solved iteratively at every point on the grid [17]. This allows electromagnetic codes to simulate induced electromagnetic effects, with time-varying electric and magnetic fields. Even though Xoopic is a 2D 3V code, the electric and magnetic fields must be known in three dimensions. Particles have velocities in three dimensions, and experience forces pushing them in this

third dimension (even if the simulation always assumes they live in a 2D plane). Moreover, the equations used in an electromagnetic solver use the curl of electric and magnetic fields in the update equations. These equations would not give valid results if the fields were only known in two dimensions.

$$\nabla \times B = \mu J + \varepsilon \mu \frac{\partial E}{\partial t} \quad (2.6)$$

$$\nabla \times E = -\frac{\partial B}{\partial t} \quad (2.7)$$

For our differentially powered *rf* plasma source, the system are powered by currents at frequencies in the MHz band, meaning that electric fields are changing on the order of MHz. There are changing electric and magnetic fields oscillating at these frequencies. Therefore, many of the physical effects in this *rf* plasma source cannot be captured by electrostatic solvers, thus it is necessary to simulate this *rf* plasma source with an electromagnetic solver.

The timestep dt is often very small in comparison to rate at which fields change, so it is reasonable to split $\frac{dE}{dt}$ into $\frac{E_{t+\Delta t} - E_t}{dt}$. The same applies for $\frac{dB}{dt}$. To store the three dimensional electric and magnetic fields, a Yee grid is used [18]. A Yee grid is a way to define electric and magnetic fields in time and space such that electric and magnetic fields are calculated asynchronously, but also such that each dimension of the three dimensional electric and magnetic fields are known at different locations of their given gridcell. This is done for stability of the simulation. In this case, electric field is computed at integer timesteps and magnetic field at half integer timesteps. To solve for electric field, Ampere's Law is used (equation 2.6). To solve for magnetic field, Faraday's Law is applied (equation 2.7). These equations are discretized below.

$$E_{t+\Delta t} = \frac{dt}{\varepsilon} \cdot \left(\frac{\nabla \times B_{t+\frac{1}{2}\Delta t}}{\mu} - J_t \right) + E_t \quad (2.8)$$

$$B_{t+\frac{1}{2}\Delta t} = -dt(\nabla \times E_t) + B_{t-\frac{1}{2}\Delta t} \quad (2.9)$$

To update the magnetic field (go from $B_{t-\frac{1}{2}\Delta t}$ to $B_{t+\frac{1}{2}\Delta t}$) the electric field is must be known at time t and magnetic field at time $t - \frac{1}{2}\Delta t$. The electric field is known in three dimensional form, and the curl can be calculated. After obtaining B at $t + \frac{1}{2}\Delta t$, the electric field can be updated. The curl of the magnetic field is calculated, and the current density (J) is known everywhere in the simulation by weighting particle currents onto a point on the grid.

These equations can be solved iteratively, but at $t = 0$, neither electric nor magnetic field is known. For this reason often a poisson solve is done at the beginning of the simulation to use the charge distribution to calculate $E(t = 0)$. Another option is to initialise magnetic and electric fields at zero and to allow them to reach a self-consistent value over a certain number of timesteps. A third option is to initialise fields to some pre decided value or function, in order to speed up convergence of the simulation.

2.6 Stability criteria for electromagnetic PIC codes

If care is not taken in setting up the initial conditions of the simulation, this can result in the simulation becoming unstable. In an unstable simulation, quantities such as plasma density, and electric or magnetic fields can increase exponentially. This is known as numerical heating [19]. In some scenarios, the plasma density and strength of the fields is seen to drop due to improper initial conditions, and this is known as numerical cooling. If incorrect initial conditions are used this can also result in a poor model of the plasma system; The

simulation executes, but converges to a steady state that is not representative of the physics occurring in the simulation. The timestep of the simulation, the grid-size and the number of particles in the simulation are crucial parameters for achieving stability in the simulation [20].

The Debye length (λ_D) of the plasma must be of the same order as the cell size in the grid [21]. This is the scale length of the plasma, and not resolving the Debye length (λ_D) will result in an inaccurate model of the plasma, and when the cell size is much greater than the Debye length ($\Delta x \approx \mathcal{O}(10 \cdot \lambda_D)$), the simulation can become numerically unstable. Plasma sheaths are often a few Debye lengths long, and cannot be resolved when the cell size is much larger than the Debye length.

A particle cannot travel a distance greater than one cell length in a single timestep. In the electromagnetic case this further restricted to a photon. This is known as the Courant–Friedrichs–Lewy (CFL) condition. If this criterion is violated, particles don't adequately respond to local fields; Information travels too far in a single timestep, leading to numerical instability.

The timestep must be small enough to resolve the plasma frequency ω_{pe} , the plasma frequency is chosen because it is often the shortest response time. However, if there is a timescale in the simulation that is shorter than the plasma frequency then the timestep must be altered in order to resolve this. Birdsall et. al [22] states that in the usual leapfrog scheme, the simulation becomes unstable when $\omega_{pe}\Delta t > 2$, however in practice the timestep is often set to values much smaller than this. This is done so that the trajectory of the electron can be adequately resolved. The electron trajectory is important as electrons drive the

change in charge density and current density. If the electron trajectories are not resolved correctly, the charge and current density are calculated incorrectly. This results in unphysical electric and magnetic fields.

A large number of particles is desirable in each cell. Statistical fluctuations are often the source of numerical heating, and having a large number of particles per cell reduces the chance of statistical fluctuations. Moreover, with a small number of particles, the velocity distribution cannot be resolved accurately in each cell, which can affect the physical results of the simulation. When starting the simulation, one must consider the trade-off between superparticle size (and consequently accuracy of simulation) and the amount of time it will take for the simulation to converge.

3 Investigation of power coupling in a differentially powered multi-tile VHF CCP using particle in cell simulation

3.1 Introduction

Low pressure radio frequency (*rf*) capacitively coupled plasmas (CCPs) are an essential tool for surface processing, such as plasma etching and plasma deposition processes in the microelectronic industry [23, 24, 25, 26], where synergistic effects of electron-driven gas chemistry, and ion-driven surface reactions enable the plasma processes. The ion flux to a surface (Γ_i) and the gas activation rate (R) are given by

$$\Gamma_i = e * n_e * v_B \quad (3.1)$$

where $v_B = \sqrt{k_B * T_e / m_i}$ is the Bohm speed, n_e is the plasma density at the sheath edge and

$$R = n_e * k_{eg} * n_g \quad (3.2)$$

where k_{eg} is the rate-constant, and n_g is the density of that chemical precursor, and n_e is the average plasma density. Loosely speaking, increasing electron density (n_e) increases both ion flux (Eqn.3.1) and chemical activation of the process gas (Eqn.3.2), resulting in increased manufacturing-tool productivity, provided the ion energy remains appropriate for the desired surface reactions.

Many challenging processes and solutions employ CCPs. The ion flux and ion impact energy are crucial parameters for many surface processes. Differing hardware solutions have been developed to optimize different processes; For example, high aspect ratio contact etch (HARC) is a plasma process often used

in the semiconductor industry, which requires a very high ion energy and high ion-flux [27]. In plasma enhanced chemical vapor deposition (PECVD) high plasma density, low ion bombardment energy, and high ion flux are desirable as they yield high processing rates and minimal substrate damage [28].

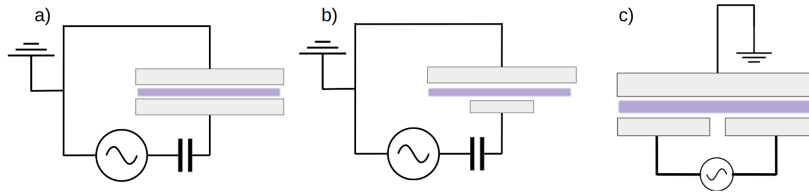


Figure 3.1: 3 geometric configurations of CCP coupling. a) shows a symmetric CCP with two electrodes of equal area. b) shows an asymmetric CCP, where one electrode has a larger area than the other. c) shows a seemingly symmetric CCP (powered to un-powered area) but where one electrode is split into two differentially powered tiles.

A CCP consists of two electrodes, with a plasma region between the electrodes. It is typical to place a 'blocking capacitor' (see Figure 1) in series with the power feed such that over an *rf*-cycle there is zero net current. Initially, due to the high mobility of electrons, the electron flux into the walls is much larger than the ion flux into the walls, giving the plasma a positive potential (with respect to the walls). The region where this potential difference exists is known as the sheath region. When tiles are driven at *rf*, the sheath approximates a capacitor where $C = \frac{\epsilon_0 A_{\text{electrode}}}{d_{\text{sheath}}}$, and $|Z| \propto \frac{1}{\omega C}$. The *rf* current in the tile is turned into displacement current in the sheath. This potential difference between the bulk plasma and the electrode boundary accelerates ions into the electrodes. A substrate can be placed on one of the electrodes and the accelerating ions in the sheath interact with the substrate when they strike the surface.

Figure 3.1 shows three different configurations of CCP. Figure 3.1(a) shows

a symmetric CCP where both electrodes have equal area. The current density at the powered electrode must be the same as the current density on the unpowered electrode, and thus the ion energy is the same at either electrode. Figure 3.1(b) shows an asymmetric CCP where the powered electrode has a smaller area than the unpowered electrode, this results in a lower current density and a smaller sheath voltage at the unpowered electrode. Placing a substrate on the larger electrode results in a lower ion energy at the substrate. The third configuration shown in Figure 3.1(c), shows a system that looks similar to the symmetric system. There are two equal area electrodes, however one of the electrodes has been split into two differentially powered tiles. The dynamics of this differentially powered system will be the focus of this paper.

In a symmetric CCP (Figure 3.1(a)), when the driving frequency is high enough ($\geq 10\text{MHz}$), the sheaths are capacitive [29] and there is a sinusoidal plasma potential oscillation ($V_p(t) = V_{p0} + \frac{V_{pk}}{2}[1 + \sin(\omega t)]$), where V_{p0} arises due to the mobility difference between electrons and ions resulting in an offset voltage between the plasma and a floating boundary. At low pressure the sheaths are collisionless and ion energy onto the boundary scales with the time averaged plasma potential. In this system, the current that flows into one electrode, must flow through the plasma and into the opposing tile; The current density, ion flux and sheath voltage at one tile is the same as the current density, ion flux and sheath voltage at the opposing tile. Increasing the power on the powered tile increases both the current density (and thus plasma density and ion flux) and voltage (and thus ion energy) at both powered and unpowered electrodes [30]. It is beneficial to have high plasma density as this increases both the chemical activation rate and ion flux (as above) at the boundaries which increases the process-rate and thus tool-productivity, provided the process is compatible with

any increase in ion energy. For many processes, including many atomic layer processes (ALPs), a lower ion energy is necessary, to prevent damaging the substrate [31, 32].

An asymmetric CCP, where the grounded electrode is larger than the powered electrode is shown in Figure 3.1(b). The current is continuous across the system, thus with the two sheaths in series (capacitive) a larger rf voltage occurs at the smaller area electrode. In steady state, this results in a large V_{rf} on the small electrode with a large negative DC bias. The large area electrode has a comparably smaller V_{rf} in comparison to the small area electrode. With this DC bias established, the electrode collects electrons over a much smaller fraction of the rf cycle, causing the plasma potential to be unperturbed for most of the rf cycle. This creates a small plasma potential oscillation (as large as T_e [3]) during the period of electron collection that moves at higher harmonics of the driving frequency [1].

Using asymmetric discharges (Figure 3.1(b)), where the one tile has a smaller area than the other tile, high rf current density and ion energy can be achieved at the small area electrode, while low rf current density and ion energy are achieved at the large area electrode. Placing the substrate on the larger electrode (often done in typical CVD systems) is, perhaps, the most used configuration of semiconductor plasma processing. Placing the substrate on the smaller powered electrode (often used in etch systems) enables high, directional (perpendicular to the substrate) ion bombardment, which enables directionality and increases etch-rate (and tool productivity) via energy deposition through the energetic ions [33]. These asymmetric discharges can be difficult to achieve for a large area substrate, particularly for small plasma volumes [34, 35, 36].

Increasing the rf frequency into the VHF band changes the sheath impedance

and gives advantages over the classically-used 13.56MHz *rf* excitation. Through particle in cell (PIC) simulation [11] it has been shown that increasing frequency into the VHF band (under constant voltage conditions) results in a higher plasma density [37], and higher current density in the plasma. It has also been observed experimentally that increasing frequency (under constant power conditions) leads to lower ion energy into the substrate, a more desirable plasma chemistry and higher ion flux. [29, 38]. Experimental work (by Abdel-Fattah, et al [39]) found that increasing the frequency (in a range from 13MHz up to 50MHz) resulted in an increasingly modified EEDF which is hypothesized to be the cause of the more-desirable plasma chemistry. Results of PIC simulation (by Sharma et al [40]) also show a modification in the EEDF as frequency increases, from bi-maxwellian at lower frequency (27MHz), transitioning to a concave EEDF (50MHz) along with an increase in plasma density at this transition frequency. Moreover, increasing frequency into the VHF band has shown superior performance in ALE and ALD applications [41, 42] One limiting factor is the wavelength of the driving frequency. As the quarter wavelength of the driving frequency approaches the electrode-length, this results in a spatial variation in the *rf*-potential, ion energy, and thus process results across the substrate [43].

To address the desire for higher frequency CCP over larger area, a new topology CCP was developed where the powered CCP electrode is divided into an array of tiles. By powering the tiles differentially ('neighbouring' tiles at 180-degree phase difference) [44] there is zero net current driven into the plasma, and zero net *rf* current at the grounded electrode. This is shown in Figure 3.1(c) [44, 1, 13, ?].

Experimentally, the differential coupling is achieved with a 1:arbitrary-N

power splitter [45] connected to the tile-array such that neighbouring tiles are 180-degrees out of phase (one output channel illustrated in Figure 1(c)). The tiles remain small, so the plasma loaded wavelength of the driving frequency is always long in comparison to the tile size. In such a plasma system, a high current density enabling high plasma density can be achieved in front of the powered tiles, while maintaining a low *rf* current density and ion energy at the unpowered substrate [1]. While plasma current moves towards one tile, plasma current moves away from the adjacent tile, meaning that the resulting *rf* current density and ion energy at the substrate remain low. Since there is no limit to the number of differentially powered tiles that can be used, this plasma is scalable to larger area substrates.

The behaviour of the currents in this plasma have been postulated and described in various conferences and publications [46, 13] but are not fully understood. In this paper we use a Particle-in-cell (PIC) simulation of this plasma, to investigate the current paths and electromagnetic fields in the plasma. A 2D, fully kinetic, electromagnetic, PIC code (Xoopic [2]) is used for these simulations.

3.2 Description of the model and plasma system

The *rf*CCP shown in Figure 3.2 is simulated using the PIC Xoopic [2] An electromagnetic solver is employed, which will capture both the electromagnetic and electrostatic fields in the plasma. In Xoopic, the boundaries of the simulation are defined (Figure 3.2) in the input file and boundary conditions are asserted depending on what type of boundary is used. The simulation is divided into a 2D grid (like in any typical PIC code), at each location on the grid, Faraday’s Law (eqn 3.3) and Ampere’s Law (eqn 3.4) are solved computationally to cal-

culate electric and magnetic fields in 3 dimensions. The electric and magnetic fields are then used to calculate a Lorentz force, which is used to update particle position and velocity. This is an electromagnetic solver, as induced electric and magnetic are considered in this type of solver. This is different from an electrostatic solver which typically solves the Poisson equation and does not consider induced electric and magnetic fields.

$$\nabla \times E = -\frac{\partial B}{\partial t} \quad (3.3)$$

$$\nabla \times B = \mu J + \epsilon\mu \frac{\partial E}{\partial t} \quad (3.4)$$

The input to the model is the 2 dimensional structure of the simulation (Figure 3.2), and the sinusoidal current waveform that drives the tile (details of this are described further in this subsection and in the appendix). More operational parameters of the simulation can be found in a table in the appendix. Electric fields, magnetic fields and particle currents in the plasma volume are self-consistent outputs of Xoopic.

The 2-D simulation boundary is an ideal conductor 200 mm wide (\hat{x}) and 40 mm high (\hat{y}) and 'infinite' in depth (\hat{z}). The top (grounded) boundary is covered with a thin dielectric to simulate a substrate for plasma treatment. Both side-walls are exposed ground surfaces enabling the system to reach a self-consistent net-charge condition independent of the starting plasma distribution. At the lower boundary there is an electrode comprised of 6 (six) tiles with surfaces exposed to the plasma. Tiles are set in a dielectric to provide isolation from the grounded, lower boundary and to exclude the plasma from the region under/between the tiles resulting in a plasma volume of 200 mm wide by 37 mm

high. Individual tiles are 25 mm wide by 1.25 mm high, and the tile-tile gap is 7 mm . The tiles are powered such that current into the back of one tile is 180 degrees out of phase with the current into the adjacent tiles. The central four tiles are powered (Tiles 2,3,4 and 5), and the two tiles near the outer walls are unpowered. The unpowered volume adjacent to the grounded boundary facilitates a self-consistent charge-balance solution for the PIC code in the sheaths and DC-bias on the powered tiles. More operational parameters can be found in the appendix. Details of this plasma volume (above $Tile_1$ and $Tile_6$) do not materially affect the behaviour (power coupling) of the plasma above the two central tiles (Tiles 3 & 4). Note that the differentially-powered, multi-tile topology CCP is fundamentally extensible by adding additional pairs of powered tiles.

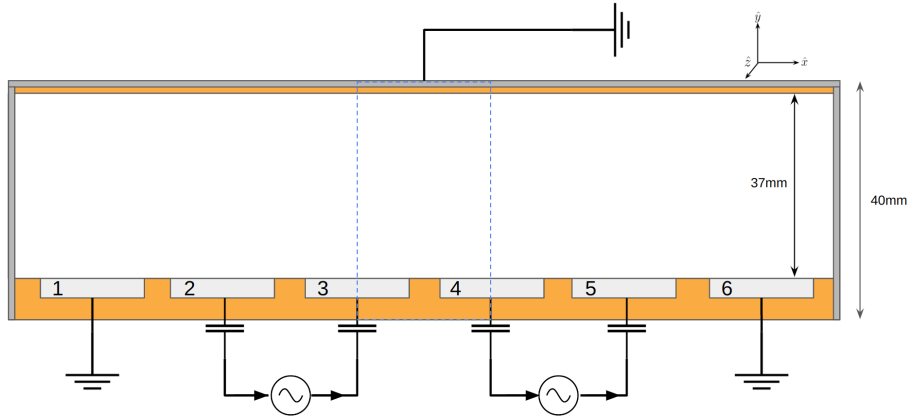


Figure 3.2: Simulated plasma chamber, analysed area in the blue dotted rectangle. Tiles labelled 1-6, and will be referred to as such.

The rf current at 160 MHz is coupled to each tile via a current-injection-region between the bottom grounded boundary and a $1\text{ mm} \times 1\text{ mm}$ metal 'stub' which is part of the under-side of the tile (more details in appendix). Figure 3.2 shows differential-coupling to pairs of tiles, as realized in experimental systems,

but in the simulation each tile is powered individually. Driving function for the central two tiles is shown below.

$$\begin{aligned} I_{T_3} &= I_0 \cos(\omega t + \pi) \\ I_{T_4} &= I_0 \cos(\omega t) \end{aligned} \tag{3.5}$$

The plasma volume (200mm x 37mm) is filled with argon gas at a pressure of 50mTorr and initialized with a uniform charge density. Electron-neutral collisions are modelled using Monte-Carlo techniques. The argon chemistry set includes only single-step ionization with a threshold energy of 15.76 eV and includes full momentum transfer cross subsections affecting electron motions. While multi-step ionization is known to affect results in VHF plasma modelling [8] we do not believe this affects the interpretation of the power coupling from tiles to plasma described below.

The simulation is run to a steady-state condition and self-consistent parameters of the plasma are determined. The average plasma density over the entire plasma volume was measured to be $5.3 \times 10^{15} / \text{m}^3$. Debye length ($\lambda_D = \sqrt{\frac{\epsilon_0 k_B T_e}{n_e e^2}}$) is $\lambda_D = 0.165$ mm. Plasma frequency ($\omega_{pe} = \sqrt{\frac{n_e e^2}{m_e \epsilon_0}}$) is $\omega_{pe} = 4.54 \times 10^9$ Hz, and the collisionless skin depth ($\delta = \frac{c}{\omega_{pe}}$) is $\delta = 66$ mm. The EEDF has a bulk population with a temperature of approximately 3.0 eV with a significant hot tail extending beyond 20 eV. Tile voltage is found to be $V_T(t) = V_{DC} + V_{rf} \sin(\omega t + \Phi)$, where V_{DC} measured to be -17V and V_{rf} was measured as 37V (Description of how V_{Tile} is determined is in the Appendix). These parameters will be considered throughout the rest of the chapter.

3.3 Power Coupling

3.3.1 Electromagnetic power coupling

Figure 3.3 shows a detailed view as highlighted in the blue-box in Figure 3.2, including the $\langle Tile_3 - Tile_4 \rangle$ push-pull pair. Red arrows in the external circuit show the rf current path at a single moment in time. Note in the push-pull configuration, at the tile-plasma boundary, current on the right half of the left tile and left half of the right tile are both in $-\hat{x}$ direction.

Currents on the top of the tiles ($I\hat{x}$) produce magnetic fields in the adjacent plasma volume ($B\hat{z}$), extending into the plasma region. Additionally, the $I\hat{y}$ on the sides of the tile (and the $I\hat{x}$ under the tile) produce a magnetic dipole in the volume between the tiles ($B\hat{z}$). For the small tiles ($l/\lambda_{rf} \ll 1$) the current is in-phase, and thus the associated magnetic fields (from all segments in this 'unit-cell' of the extensible plasma source) are in-phase. Under a 1st-order approximation that the plasma density and plasma-boundary position are constant across the face of the tile, then the magnitude of the tile-current scales linearly from zero at the tile-center to a maximum at the tile-edge. The rf magnetic field above the tiles scales with the rf current on the tile face. For the geometry presented here the dipole magnetic field has the same amplitude as the tile-edge magnetic field. Evaluating the magnetic field in the first-cell above the tiles/dielectric, $B_z(x)$ has approximately the following functional dependency:

$$B_z(x) = \left\{ \begin{array}{ll} 2.5 \times 10^{-6} \text{ T} * \frac{x}{12.5 \text{ mm}} & x \in [0 \text{ mm}, 12.5 \text{ mm}] \\ 2.5 \times 10^{-6} \text{ T} & x \in [12.5 \text{ mm}, 19.5 \text{ mm}] \\ 2.5 \times 10^{-6} \text{ T} * \frac{-(x-32)}{12.5 \text{ mm}} & x \in [19.5 \text{ mm}, 32 \text{ mm}] \end{array} \right\} \quad (3.6)$$

where the center of $Tile_3$ is defined at $x = 0$ mm, and the center of $Tile_4$ is defined at $x = 32$ mm. As a point of reference, at the first cell above the dielec-

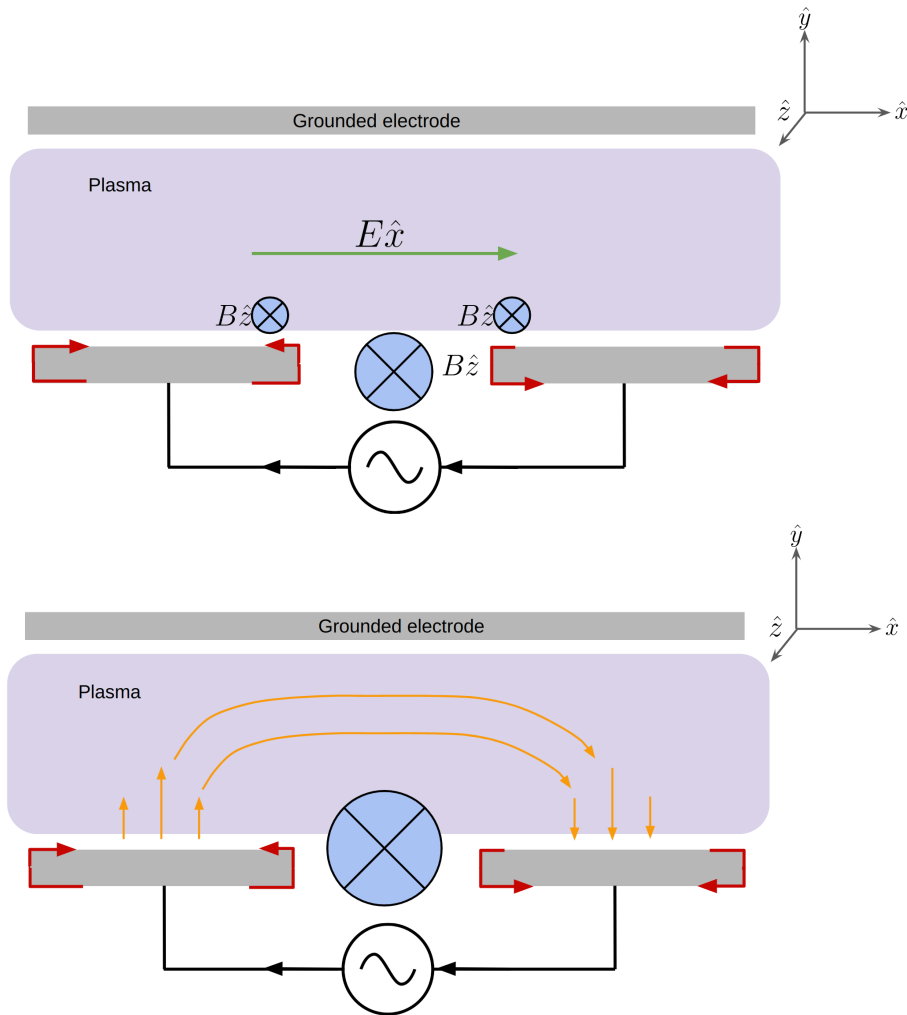


Figure 3.3: (a) Magnetic fields generated by currents on the surface of electrodes, induced electric field due to time varying magnetic field. Red arrows show currents travelling on the surface of the tile. (b) Current coupled from one tile to adjacent tile due to the induced electric field created by the magnetic field between the tiles. The orange arrows represent the current path due to the induced EMF created by the changing magnetic field.

tric in the center of the tile-tile gap the magnetic field approaches 3.0×10^{-6} T. This is attributed to *rf* currents on the side of the tile (facing tile-tile gap) contributing to the magnetic field).

By Faraday's law ($\nabla \times E = -\frac{\partial B}{\partial t}$), this changing magnetic dipole induces a horizontal electric field (E_x in Figure 3.3(a)) in the plasma, driving plasma current in the \hat{x} -direction. This plasma current connects the plasma volume above one tile to the plasma volume above an adjacent tile. The current path is shown in Figure 3.3(b), and will be referred to as the 'coupled current' from now on. In the conductive plasma the magnetic field is limited to the boundary of the plasma with scaling of the collisionless skin depth $\delta = \frac{c}{\omega_{pe}}$ convoluted with the near-field scaling of the spatially-restricted magnetic dipole ($\tilde{B} = B_1(\frac{y}{s})^2$) where s gives the scaling parameter, somewhere between the tile-tile-gap (the space between adjacent tile edges where the vacuum magnetic field is observed) and the tile-center to tile-center distance [47].

3.3.2 Electrostatic power coupling

There is also a purely electrostatic phenomenon occurring in the plasma boundary region adjacent to the tile-face which causes a local oscillation in the plasma potential. With adjacent tiles being 180-degrees out of phase with each other, there is an $rf-V_p$ at one tile which is out-of-phase with an $rf-V_p$ at the adjacent tile. This results in a plasma potential difference between the volume in front of *Tile*₃ vs *Tile*₄. This potential gradient results in an electric field which drives current in the \hat{x} -direction, parallel to the plasma boundary.

The origin of the plasma potential oscillation comes from the fact that an individual tile operates as a small, asymmetrically powered electrode, and the observation that the powered tiles take on a DC bias potential. Thus the period of the rf oscillation during which electrons are collected (to balance the ion charge collected uniformly over the rf cycle) is reduced. This can result in a momentary positive-swing in the sheath-edge plasma potential exactly when the tile passes through the peak voltage and electrons are being drawn from

the plasma. This typically occurs with large *rf* voltages and large DC-biases (and thus very short electron collection) and thus the 'burst' of electron current required affects the local plasma potential. This is also seen in plasmas with light ions, such that the *rf*-period averaged ion charge is comparably large, and so-called field-reversal has been observed [48, 49].

The differentially powered plasma system does not, at first glance, suggest field reversal should be a significant result for the heavy mass ions and relatively small *rf* and dc voltages. However, the *rf* frequency is only a factor of 4.5 below the average plasma frequency. The typical approximation of $\omega_{rf} \ll \omega_{pe}$ no longer holds, and the inductance of the plasma electrons becomes more significant; A local penetration of external electric field into the plasma beyond the sheath seems realistic and the perturbation would be expected to be as large as T_e [3]. Note this is a purely electrostatic phenomena. The *rf*-phase for the peak plasma potential oscillation is at the peak tile voltage, which is 90-degrees delayed from the peak current; That is, the electrostatic field is in-phase with the electromagnetic field. Consider a moment in *rf*-phase when V_{T3} is a maximum negative value ($-54V$) and the plasma potential profile would match the pre-sheath \hat{y} shape to satisfy the Bohm criterion; At this same moment V_{T4} is at a maxima ($+20V$) which could be as much as T_e greater than the quiescent value of the floating potential, V_{p0} , where V_{p0} without *rf*-current in the sheaths should be $15V$. A first approximation of the plasma potential oscillations would be a sinusoidal oscillation combined with a 3rd-harmonic to temporally restrict the period over which the perturbation in V_p occurs. (The plasma frequency is higher than the third harmonic, but lower than the 5th harmonic.) The resultant current in the \hat{x} -direction is in phase with, and in the same direction with, the EM-"coupled-current" so both phenomena need to be considered when talking about "coupled current".

3.3.3 Plasma density

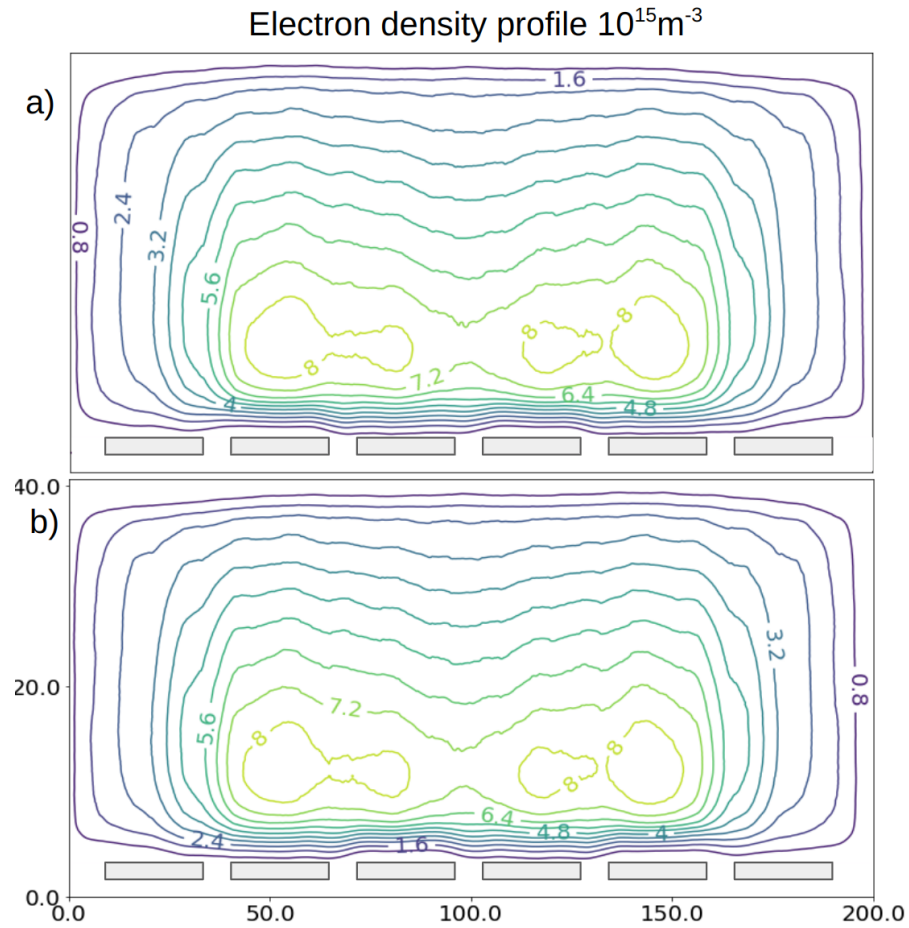


Figure 3.4: Contour plot of electron density in the plasma volume at two moments in the *rf* cycle; a) Voltage on tile 3 is at a maximum, b) voltage on tile 4 is at a maximum. A very small change in density ($\approx 1\%$) in plasma in front of adjacent tiles is observed over the *rf* cycle.

A contour plot of the electron density in the plasma volume is displayed in Figure 3.4. The location of the tiles has been edited into the plot for clarity. Figure 3.4(a) shows plasma density when current into *Tile*₃ and *Tile*₅ is at a maximum, and current into *Tile*₂ and *Tile*₄ is at a minimum. Figure 3.4(b) shows plasma density when current into *Tile*₂ and *Tile*₄ is at a maximum, and

current into $Tile_3$ and $Tile_5$ is at a minimum. In both plots the average plasma density is $5.3 \times 10^{15} m^{-3}$. A higher plasma density is observed near the powered tiles, reaching almost double the average plasma density. This is where most of the plasma current density moving away from the tiles changes direction and becomes coupled current. Towards the substrate ($y=40\text{mm}$), the plasma density decreases. In the plasma volume in front of $Tile_1$ and $Tile_6$, the plasma density decreases rapidly.

Observing plasma density in front of the two central tiles, the plasma density in front of $Tile_3$ is similar to the plasma density in front of $Tile_4$. When measured over the rf cycle, there is little variation in the plasma density in front of these tiles (only varies by approximately 1%).

3.4 Currents and magnetic fields

To understand the behaviour of the current coupling between two differentially powered tiles, the region encompassing the two central tiles, and extending across to the grounded surface (Figure 3.2, blue box) is analysed. Figure 3.5 shows (a) Current in the \hat{x} -direction, (b) current in the \hat{y} -direction and (c) magnetic field in the \hat{z} -direction at the point in the rf cycle when current into the back of $Tile_4$ is at a maximum. Current shown in Figure 3.5 is conductive current due to ion and electron motion (and does not show the displacement current, thus the sheath region above the tiles, and the region containing dielectric material are current free). As voltage-gradients in the bulk- plasma are small, there is no charge accumulation, so the currents must be continuous. Figure 3.6 shows the currents from Figure 3.5(a) and (b) in a quiver plot at 3 different moments in the rf cycle.

Observing Figure 3.5(b), current is driven into the $Tile_4$, converted into displacement current in the sheath and back into conductive current which moves

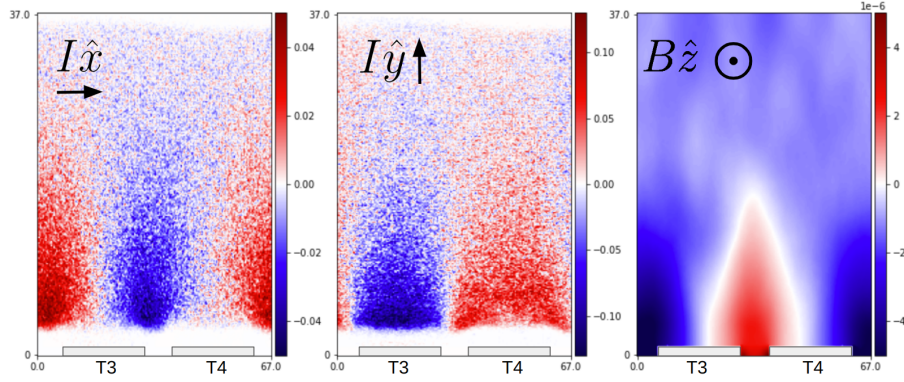


Figure 3.5: *rf* current in (a) the \hat{x} direction, (b) the \hat{y} direction, and (c) magnetic field in \hat{z} direction between the two central tiles at the same point in time.

across the plasma in the \hat{y} -direction toward the grounded boundary (Figure 3.5(b), *Tile*₄). Some of the current is converted into current in the \hat{x} -direction (Figure 3.5(a), between *Tile*₃ and *Tile*₄). The current in the \hat{x} -direction is converted back into current in the negative \hat{y} -direction Figure (3.5(b), *Tile*₃), which combines with a minority of current moving from the grounded boundary above the *Tile*₃, coupling into *Tile*₃. Current in the \hat{y} -direction is at its strongest in front of the tiles close to the sheath edge. Moving further into the plasma, the current in the \hat{y} -direction decreases, meaning that the current changes direction into the \hat{x} -direction. This is consistent with the Figure 3.5(a) showing current in the \hat{x} -direction. There is a current in the $-\hat{x}$ -direction between the two central tiles, showing a current parallel to the face of the tiles, this is the aforementioned ‘coupled current’. Observing current in \hat{y} -direction in Figure 3.5(b), it can be seen that there is a current which travels from the tile, to the substrate. Not all the current couples between adjacent tiles. Some of the current makes it to the other side of the plasma where it reaches the grounded substrate.

In Figure 3.5(c) it can clearly be seen that there is a dominant magnetic field in the \hat{z} -direction between the tiles. This is due to the electromagnetic coupling

mechanism described earlier (Figure 3.3). The magnetic field is strongest near the tiles, and then decays as it moves into the plasma, due to the skin depth of the plasma, and the scaling length due to the size of the magnetic dipole. On the far right and far left sides of Figure 3.5(c), there are 2 regions with large magnetic fields in the opposite direction. This is due to electromagnetic coupling occurring between tiles 2 and 3 on the left, and tiles 4 and 5 on the right, (tiles 2 and 5 are not in frame of the plot). These magnetic dipoles are 180 degrees out of phase with the magnetic dipole created between the Tiles 3 and 4.

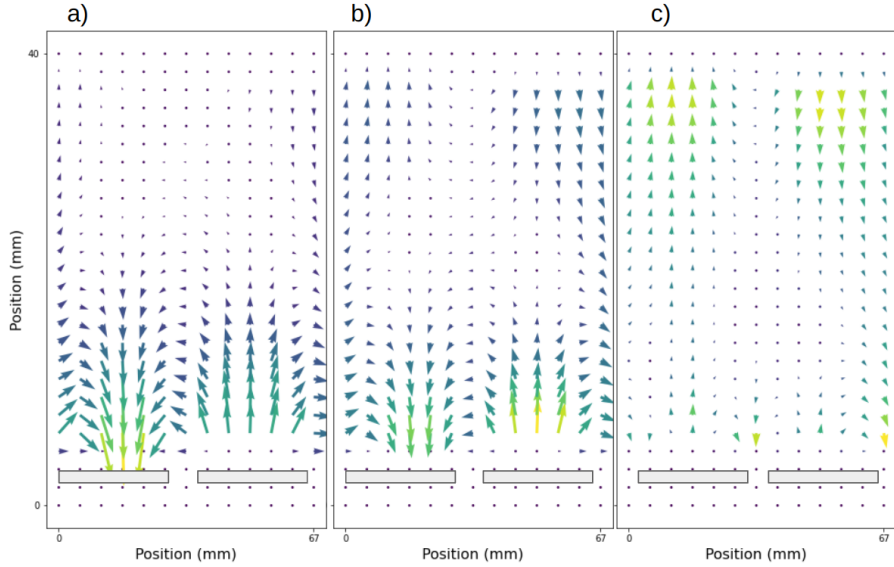


Figure 3.6: Current path in simulation at three different phases. Figure 3.6(a) is when current into the tiles is maximal at 0 degree phase ($Tile_3$ powered with current waveform $I(t) = I_0 \sin(\omega t + \phi)$). Figure 3.6(c) shows current at 90 degree phase, when there is no coupled current between adjacent tiles. Figure 3.6(b) shows the transition between these two phases (45 degrees)

To further illustrate the current path of the plasma, the current path between the central tiles is shown in a quiver plot in Figure 3.6, at three different moments in the rf cycle ($\phi = 0, \phi = \pi/4$ and $\phi = \pi/2$. $\phi = 0$ is defined as the

moment in time where the current into $Tile_4$ is maximal). The arrows represent the instantaneous current vector at that location in the simulation (again, it is showing only conductive, particle current, and does not include displacement current in the sheaths). Looking at Figure 3.6(a), it can be seen that plasma current couples from the $Tile_4$ to $Tile_3$. Above $Tile_4$, plasma current is pushed into the plasma. In the region between the tiles, the current has changed direction and the coupled current is seen, moving parallel to the face of the tiles. As this current approaches $Tile_3$, it changes direction again and points towards $Tile_3$. 80% of the plasma current driven at the sheath edge, changes direction and turns into coupled current parallel to the face of the tile, while only 20% of the current pushed out makes it to the substrate.

Figure 3.6(b) is the intermediate state between maximal current coupling in the plasma and minimal current coupling in the plasma. This shows the moment of time in the rf cycle where current into the back of $Tile_4$ is decreasing. This is at phase $\phi = \pi/4$, meaning that current amplitude is 0.707 of the maximum value. This is reflected by a decreasing current in the plasma at the sheath edge and there is a smaller amount of coupled current. A small rf current at the grounded tile is starting to build up. Figure 3.6(c) shows conductive current in the plasma at a phase where the current into the tile is at minimum. At this moment $Tile_3$ is at a minimum in voltage and $Tile_4$ is at a maximum in voltage.

3.5 Power coupling in the plasma

To further understand the power coupling phenomena, the horizontal electric field, coupled current and tile voltage from Xoopic were analysed over an rf cycle. Spatial average magnitudes are calculated by averaging over a region 11mm wide and 10mm high centered on the tile-tile boundary and extending vertically from the sheath edge into the plasma. This region is chosen to measure horizontal

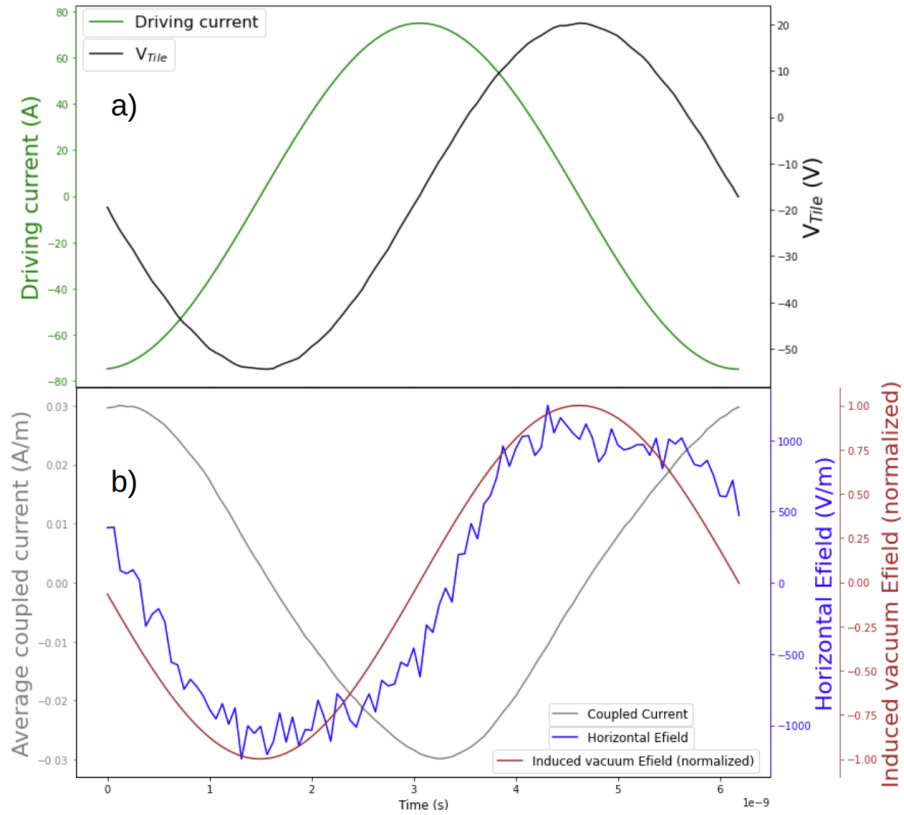


Figure 3.7: a) tile voltage and driving current over an *rf* cycle, b) coupled current, horizontal electric field and induced electric field over an *rf* cycle

electric field and coupled current, as this is the region between the plasma where current coupling is the strongest (see Fig.3.5).

Figure 3.7(a) shows $Tile_3$ driving current in green and voltage in black. V_{Tile} is sinusoidal and is observed to lag the driving current by 89.47 degrees. In Figure 3.7(b) average coupled current is plotted in grey, and average horizontal electric field in blue. In brown, the theoretical induced electric field is shown (Electrostatic and electromagnetic cannot be separated in Xoopic, so this is the vacuum field as derived from the current using Faraday's law), which lags the driving current by 90 degrees. The horizontal electric field lags the voltage on the tile and vacuum electric field by 7 degrees. The coupled current lags the

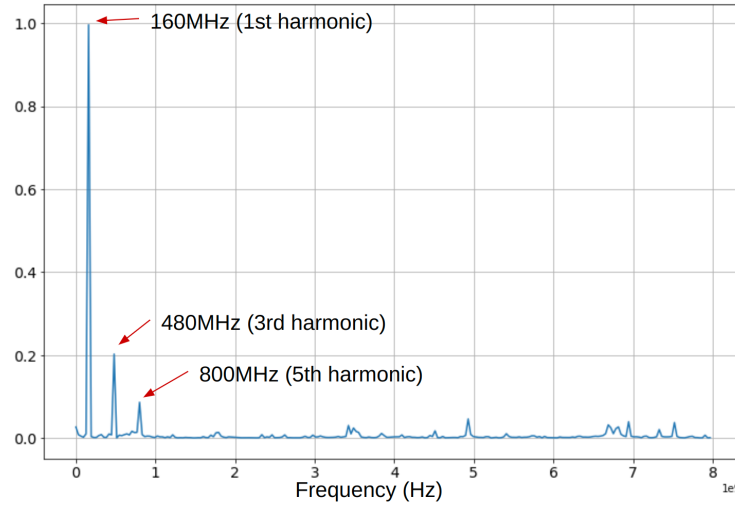


Figure 3.8: Result of a fourier transform of horizontal electric field, showing relative amplitude of frequencies.

horizontal electric field by 75 degrees, meaning that the coupled current is inductive, due to inertia of electrons in the plasma. The coupled current is 173 degrees out of phase with the current into the right tile, and it is 7 degrees out of phase with the current into the back of the left tile. This means that there is a continuous current path for plasma current moving away from one tile, changing direction to move parallel to the face of the tile and then into the sheath at the face of the adjacent tile.

horizontal electric field was observed over 5 *rf* cycles, and a Fourier transform was performed. The output of the Fourier transform is shown in Figure 3.8. As expected, the horizontal electric field is dominantly first harmonic, oscillating at the driving frequency. The measured electric field has a significant third harmonic component ($\approx 20\%$) and some fifth harmonic ($\approx 7\%$). These harmonics attributed to asymmetry in V_p in front of the tiles during the part of the *rf* cycle when the tile voltage reaches V_{max} , which is of electrostatic origin, described in

the introduction.

3.6 Plasma response at a differentially-powered tile-pair

The question remains whether the coupled current is driven by the electrostatic variation in plasma potential or the electromagnetic phenomenon. To answer this question a simplified plasma model, Generalized Ohm's Law is employed. This model assumes that displacement current is zero, thus it is an electrostatic approximation. If horizontal electric field and coupled current in the plasma can be described by this model, it can be determined that these fields can be of electrostatic origin. To further determine wwhich phenomenon drives the coupled current, Faraday's Law is solved in the plasma volume in front of the tile-tile pair, to determine if the induced electric field is of comparable size to the electric fields observed in the plasma.

3.6.1 Generalized Ohms law

Generalized Ohm's Law can be derived from electron and ion equations of motion [50], assuming quasi-neutrality, and that $\frac{dE}{dt} = 0$. In a bulk plasma quasi-neutrality can be assumed, and if the electric field is of electrostatic origin, then the displacement current would be zero. Beginning at the electron and ion equations of motion:

$$\frac{d}{dt}(n_e m_e u_e) + \nabla \cdot (n_e m_e u_e u_e) = -\nabla \cdot P + en_e (E + u_e \times B) + R_e \quad (3.7)$$

$$\frac{d}{dt}(n_i m_i u_i) + \nabla \cdot (n_i m_i u_i u_i) = -\nabla \cdot P + en_i (E + u_i \times B) + R_i \quad (3.8)$$

In the bulk plasma, The gas pressure is low ($P = 50mT$), so the pressure

term in this equation can be neglected. The magnetic fields are small enough that the $u \times B$ term in the Lorentz Force can be neglected. Current is continuous in the bulk plasma with no sources or sinks meaning that $\nabla \cdot J = 0$. This means that the divergence term in the equations of motion can be assumed to be zero. The remaining terms in the equations of motion are combined:

$$m_e \frac{d}{dt} (n_i u_i - n_e u_e) = e \left(n_e + \frac{m_e}{m_i} n_i \right) \cdot E - R_e \quad (3.9)$$

The bulk plasma is quasi-neutral ($n_i \approx n_e$) and ions are slow in comparison to electrons. This means that $n_i u_i - n_e u_e$ can be expressed as $n_e u_e = -\frac{J}{e}$, where J is the current density. R_e is the rates of change of electrons ions due to collisions, and can be expressed as $R_e = \nu_c J$. Subbing into the previous equation results in Generalized ohms law (equation 3.10. Note that the plasma frequency is $\omega_{pe} = \sqrt{\frac{n_e e^2}{m_e \epsilon_0}}$).

$$\frac{dJ}{dt} = \epsilon_0 \omega_{pe}^2 E - \nu_c J \quad (3.10)$$

Using outputs from Xoopic (electric fields and currents), we can evaluate whether the Xoopic results fit this electrostatic approximation. $\omega_{pe} = 4.54 \times 10^9 Hz$ is the previously calculated plasma frequency, $\nu_c = 2 \times 10^8 Hz$ is the electron collision frequency [51]. This equation is applied to the horizontal electric field, and coupled current shown in Figure 3.7(b). Sine waves are fitted to electric field and coupled current. From this fit, expressions for $J(t)$, $\frac{dJ(t)}{dt}$, and $E(t)$ are determined. Note, that the coupled current shown in Figure 3.7(b) is current in the x-direction in that particular cell and must be divided by the cell height (0.156mm) to calculate coupled current density, yielding a current density amplitude of $192 A m^{-2}$.

$$\nu_c \cdot J(t) = 2 \times 10^8 \cdot 192 \sin(\omega t) = 3.84 \times 10^{10} \sin(\omega t) [Am^{-2}s^{-1}] \quad (3.11)$$

$$\begin{aligned} \varepsilon_0 \cdot \omega_{pe}^2 \cdot E(t) &= 8.85 \times 10^{-12} \cdot 4.54 \times 10^9 \cdot 1140 \sin(\omega t - 1.3) \\ \varepsilon_0 \cdot \omega_{pe}^2 \cdot E(t) &= 20.4 \times 10^{10} \sin(\omega t - 1.3) [Am^{-2}s^{-1}] \end{aligned} \quad (3.12)$$

$$\frac{dJ(t)}{dt} = 192 \cdot \omega \cos(\omega t) = 19.2 \times 10^{10} \cos(\omega t) [Am^{-2}s^{-1}] \quad (3.13)$$

These expressions were applied to equation 3.10, and the terms containing $J(t)$ and $\frac{dJ(t)}{dt}$ were summed together. The result is plotted in Figure 3.9. If the red curve and the blue curve are equal, then Generalized Ohm's law is satisfied, meaning that the coupled current and horizontal electric field fit the electrostatic approximation. The two curves are almost in phase (4 degrees out of phase), the amplitude of the two curves differs by 5%. This is a very good fit signaling that the electrostatic approximation may be a good description for the electric fields and currents in the plasma system. There are some approximations in this calculation. The plasma density is considered to be the average plasma density, but as shown in Figure 3.4, the electron density is larger near the powered electrode than towards the unpowered substrate. The electron collision frequency is an approximation and is determined by the electron temperature and experimentally measured cross-sections. The horizontal electric field and coupled current are approximated as sine waves, but realistically they are not perfect sine waves. These approximations add some error to the calculation. To further explore whether we can fit this equation to the results of the Xoopic simulation, an analytical model of Generalized ohms law is developed.

An analytical model of Ohm's Law is created and fitted to Xoopic simulation results. This model solves the following equations to determine expressions for Current density and electric field.

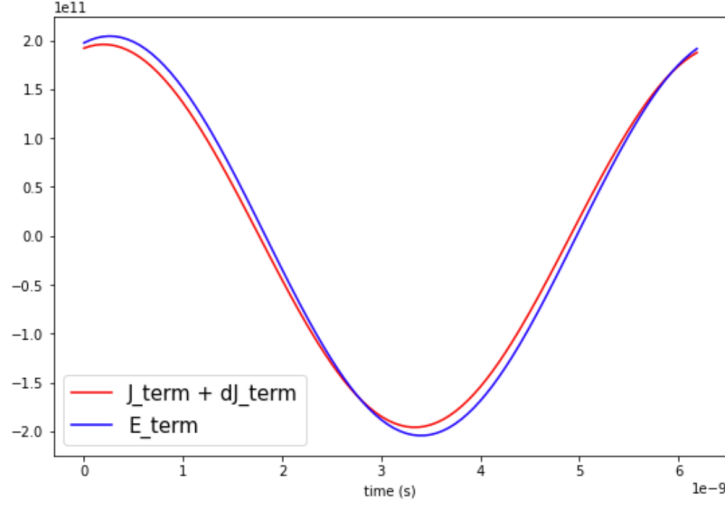


Figure 3.9: Terms from Generalized Ohms law plotted. The red curve shows the combination of the $\frac{dJ}{dt} + \nu_c J$, and the blue curve plots $\varepsilon_0 \omega_{pe}^2 E$. The curves are almost equal, showing the model is a good fit.

The electrostatic approximation of Ampere’s Law, omitting displacement current,

$$\nabla \times B = \mu_0 J \quad (3.14)$$

Faraday’s Law,

$$\nabla \times E = \frac{\partial B}{\partial t} \quad (3.15)$$

And Generalized Ohm’s Law.

$$\frac{dJ}{dt} = \varepsilon_0 \omega_{pe}^2 E - \nu_c J \quad (3.16)$$

Resultant fields are calculated in 2 dimensional space, to enable comparison to the 2D fields in Xoopic. This model asserts an expression for magnetic field, which is based on an observation of the self-consistent magnetic field from the Xoopic simulation. B_z at the tile face is periodic over the tile-center spacing

($B_z(x) \propto \cos(\frac{2\pi x}{L})$). The decay of B_z into the plasma has two components, a component due to the periodic nature of the dipoles, and due to the skin depth-shielding. Combining all expressions, results in the approximation of $B_z(x, y, t)$.

$$B_z(x, y, t) = \cos\left(\frac{2\pi x}{L}\right) \cdot \exp\left[-\sqrt{\left(\frac{2\pi}{L}\right)^2 + \left(\frac{1}{\lambda_{SD}}\right)^2}\right] y \cdot \exp i\omega t \quad (3.17)$$

Where L is a characteristic length in x-direction, and λ_{SD} is the skin depth in the plasma.

In Figure 3.10 the resulting current densities from the analytical model are compared to currents from the Xoopic simulations. The y-profile of the currents from the analytical model are compared to the y-profile of the currents in the Xoopic simulation. Currents in the y-direction are calculated at the tile-center, in a region 10 cells wide stretching from $y=8\text{mm}$ to $y=40\text{mm}$. Currents in the x-direction are calculated in the center of the tile-tile gap in a region 10 cells wide stretching from $y=8\text{mm}$ to $y=40\text{mm}$.

In Figures c) and d) the pattern shows a four-fold symmetry. Current moving away from or towards adjacent tiles, with 180 degree phase shift between adjacent tiles. In Figures a) and b), coupled current is observed between adjacent tiles. In both the x-direction and the y-direction, the Xoopic current shape matches the shape of the output of the Generalized Ohm's Law model. The y-profile of the current both in the x-direction and y-direction accurately fits the electrostatic approximation. This suggests that the electrostatic approximation can describe the current path observed in the Xoopic simulation, and implies that the dominant mechanism for driving the coupled current is due to the variation in electric potential.

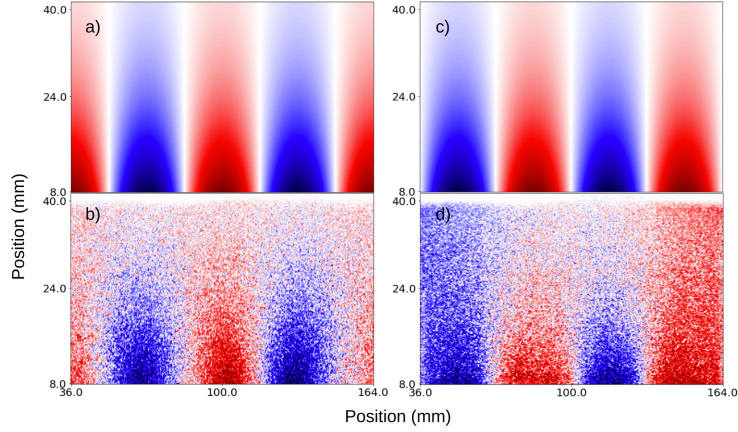


Figure 3.10: Analytical model current densities compared to self-consistent Xoopic currents.(a) J_x from the analytical model, (b) J_x from Xoopic simulation,(c) J_y from the analytical model, (d) J_y from Xoopic simulation driven at 75A/m.

3.6.2 Faraday's Law solution

To further understand whether the horizontal field is due to the electrostatic or electromagnetic phenomenon, Faraday's Law is solved in the system, along the coupled current path. The equation is displayed below.

$$\begin{aligned} \nabla \times E &= -\frac{\partial B}{\partial t} \\ \frac{\partial E_x}{\partial y} - \frac{\partial E_y}{\partial x} + \frac{\partial B_z}{\partial t} &= 0 \\ E_x \cdot L - 2E_y \cdot H + \iint_S \frac{\partial B_z}{\partial t} \cdot da &= 0 \end{aligned} \quad (3.18)$$

The reason to solve this equation is to compare the strength of the induced EMF from the time-varying magnetic field to the strength of the electric fields observed in the Xoopic simulation. If the induced electric field from the time-varying magnetic field is much smaller than the electric fields in the Xoopic simulation, then the electromagnetic phenomenon cannot be the dominant phenomenon for driving the coupled current. The three terms in this equation can be calculated using Xoopic output electric and magnetic fields.

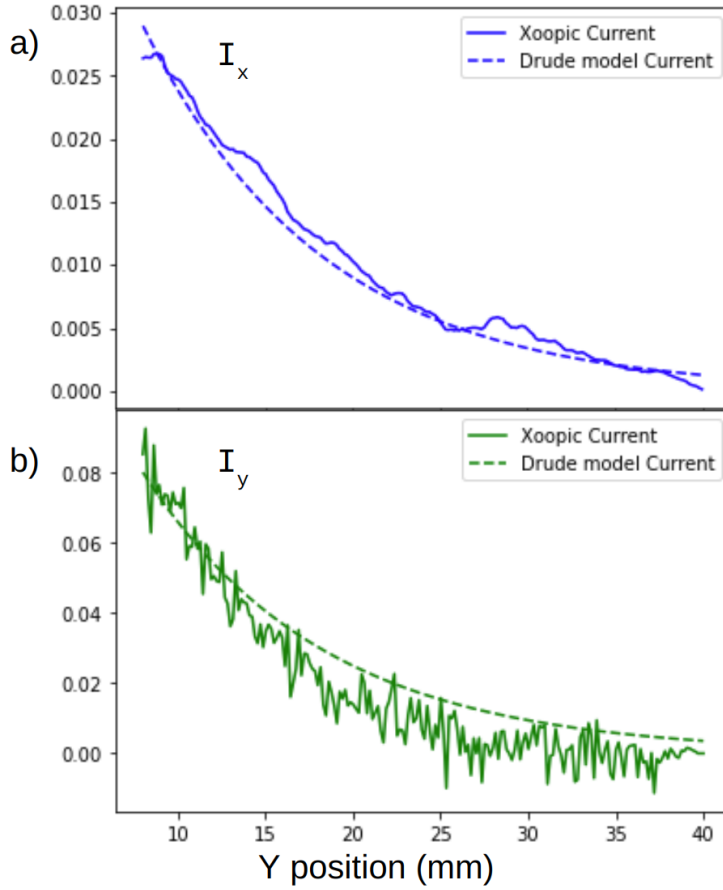


Figure 3.11: Y profile of currents in analytical model vs Xoopic simulation.

A rectangle is defined spanning from the tile-center of $Tile_3$ to the tile center of $Tile_4$ (32mm) extending 16mm into the plasma shown in Figure 3.12. Faraday's Law is solved in this region. Electric field in the y-direction has been calculated as the average electric field from 8m in the plasma to 16mm in the plasma. Electric field in the x-direction was calculated as the average electric field from the tile-center of $Tile_4$ to the tile-center of $Tile_3$ at $y=16$ mm. When solving Faraday's Law in this system, only the z-component of the equation is

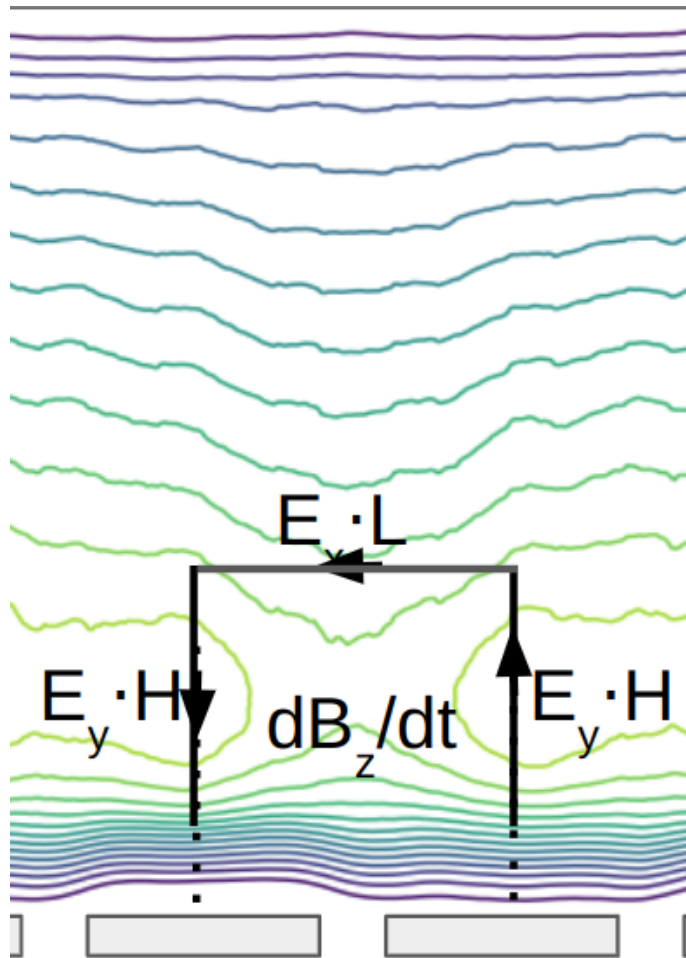


Figure 3.12: Path where Faraday's Law is solved, with enclosed magnetic field.

considered, as this is the only component with significantly large values.

The resulting fields are shown in Figure 3.13. sine waves have been fitted to all curves, with respective amplitudes calculated. The amplitude of the individual components of equation 3.18 are shown below.

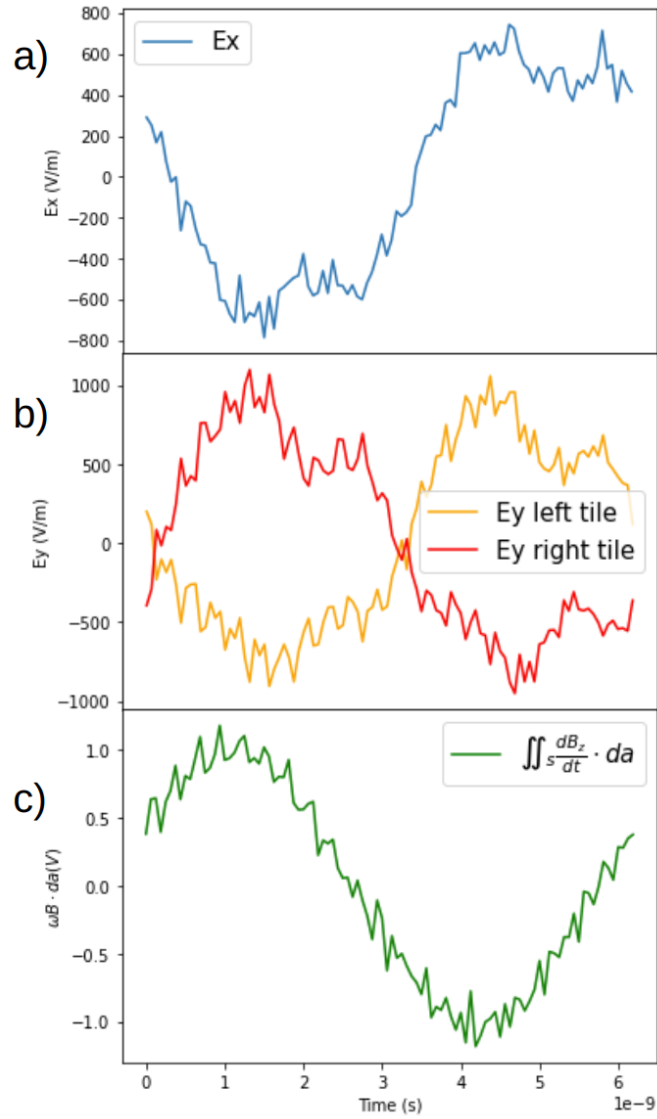


Figure 3.13: (a) Electric Field in the x direction, (b) electric field in the y direction and (c) Time derivative of the enclosed magnetic field ($\omega B \cdot da$).

$$\begin{aligned}
 E_x \cdot L &= 710\text{V/m} \cdot 0.032\text{m} \approx 23\text{V} \\
 -2 \cdot E_y \cdot H &= 2 \cdot 770\text{V/m} \cdot 0.016 \approx -24\text{V} \\
 \iint_S \frac{\partial B_z}{\partial t} \cdot da &= 1.2\text{V}
 \end{aligned}
 \tag{3.19}$$

The induced EMF from the time varying electric field is 1.2V which is much smaller than the voltage across the plasma due to the fields observed in Xoopic (23V and -24V, a factor of 20 larger than the induced field) in the x-direction and y-direction respectively. It can be concluded that the horizontal electric field, and coupled current fit the electrostatic approximation, with minimal influence from the electromagnetic phenomenon.

Note that in the electrostatic approximation, the terms containing electric field should be equal. However there are various sources of error in this calculation. The electric fields are averaged in a region of space and are assumed to be sinusoidal. We know there are some higher harmonics in the electric field which is especially evident when observing the electric field in the y-direction. However, the point remains that the electric fields observed are too large to be described by the electromagnetic phenomenon.

4 Variation in plasma coupling with drive current

4.1 Introduction

In Chapter 3, a differentially powered, VHF plasma system was described. A 'coupled current' path was found in the plasma that couples plasma current from one tile to the adjacent tile, and it was determined that this current path came due to two physical phenomena; an electrostatic phenomenon, caused by a spatio-temporal variation in the plasma potential, and an electromagnetic phenomenon caused by a time-varying magnetic field in the space between two tiles. To understand this plasma system better there is a need to see how the plasma changes, under changes in input conditions. Harvey et. al [1] have shown experimentally how some of the diagnostics in such a differentially powered system evolve over time, but many of the scaling laws have never been investigated for the comparably low voltage for the differentially powered VHF plasma system.

In this chapter we will investigate the plasma response, and in particular the nature of the plasma currents as a function of the amplitude of the *rf* tile currents. A detailed description of the plasma system is given in Section 3.2. The plasma system remains the same, but driving current is varied between 25A and 175A.

4.2 Low current and high current experiments

The plasma volume shown in Figure 3.2 is simulated using Xoopic [2] and the behaviour of the plasma with change in amplitude of drive current is observed. In Figure 4.1, diagnostics of a 'low current' simulation driven at 50A per tile is observed. This figure shows current in \hat{x} -direction, current in the \hat{y} -direction, magnetic field in the \hat{z} -direction and plasma density in the plasma volume above

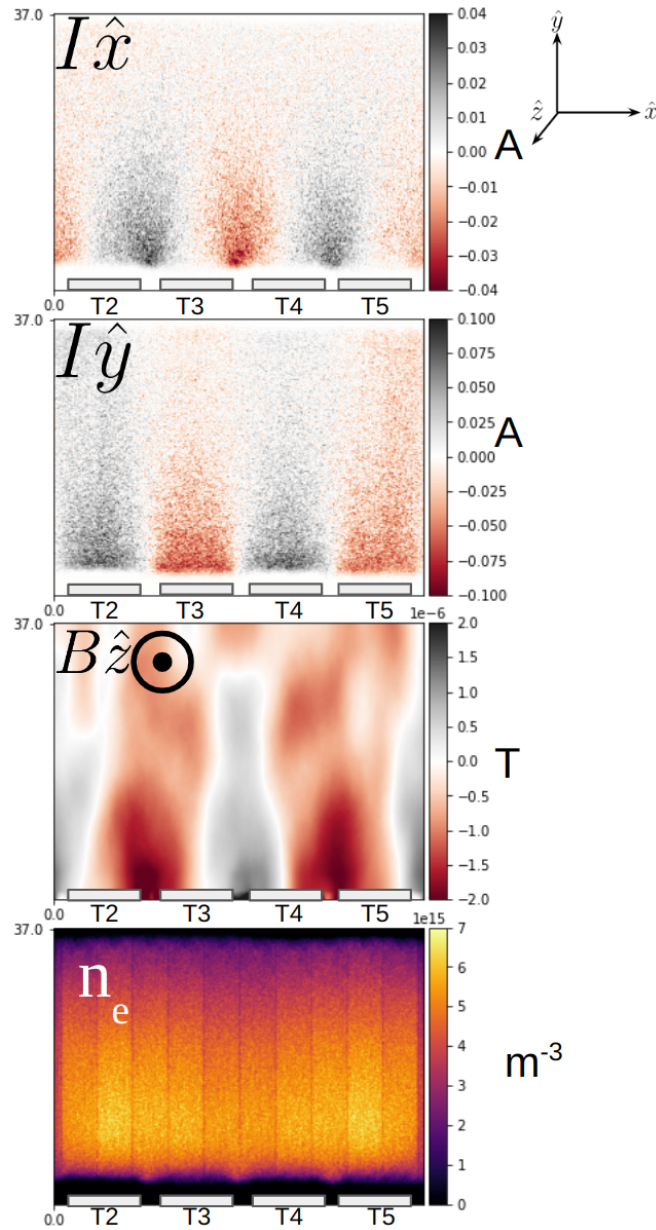


Figure 4.1: 2D profiles across the center 4 tiles for a simulation driven at 50A. Current in (a) x-direction, (b) y-direction, (c) Magnetic field in z-direction and (d) electron density. Currents and magnetic fields are defined as the total current or magnetic field in that particular cell.

the central 4 tiles (with tiles labelled accordingly, $Tile_1$ and $Tile_6$ are out of frame, an image of full simulation is shown in appendix).

In Figure 4.1(a)(b)(c), the power coupling discussed in the Section 3.3 is observed. At this moment in time current is pulled out of the back of tiles 3 and 5 and current is pushed into tiles 2 and 4. This results in plasma current moving away from the tiles into the plasma at tiles 2 and 4 and towards the tiles at tiles 3 and 5 (seen in Figure 4.1(b)). Tiles 1 and 6 are driven at low current (5% the magnitude of other tiles), to avoid strong effects between the plasma and the walls (on the left and right) impacting the plasma in the volume at the central 4 tiles. Plasma current moving away from tiles 2 and 4 changes direction and moves horizontally, parallel to the face of the tiles (coupled current). This is seen in the currents in the \hat{x} -direction (Figure 4.1(a)). In the region between tiles 3 and 4, plasma current moving away from $Tile_4$ moves in the $-\hat{x}$ -direction towards $Tile_3$. This current then joins the current moving towards $Tile_3$. This forms a complete current path coupling current from $Tile_4$ to $Tile_3$. Current density of the coupled current decreases with distance from the tile. The same current coupling occurs between adjacent tile-tile pairs. There is also some current that crosses the plasma to the grounded electrode at $y=4\text{cm}$. We will refer to this current as 'substrate current'.

Observing magnetic field in the \hat{z} -direction (Figure 4.1)(c)), magnetic dipoles are seen between adjacent tile-tile pairs, these magnetic dipoles are created by rf currents on the surface of the tiles, and are thus rf oscillating magnetic fields themselves. In the gap between tiles 3 and 4 magnetic field points out of the page, and in the space between tiles 2 and 3, and between tiles 4 and 5 magnetic field points into the page. These time-varying magnetic fields create an induced electric field. Magnitude of magnetic field decreases as a function of distance from the tiles, which is consistent with the decrease in coupled current density

as a function of y-position.

Electron density is displayed in Figure 4.1(d). There are distinct vertical lines in the electron density; This is an artefact of multi-threading in Xoopic, and we believe that it does not affect the physics in the simulation (discussed in the appendix). Plasma density is higher near the powered tiles. This is where most of the plasma current density moving away from the tiles changes direction and becomes coupled current. Towards the substrate ($y=4\text{cm}$), the plasma density is lower.

In contrast, Figure 4.2 shows results of a 'high current' simulation driven with 150A of driving current amplitude per tile. Note that the same plots have been used, but scale of each of the plots has been changed.

In the 'high current' simulation current is coupled between adjacent tiles similarly to the 'low current' simulation. However there are some differences in the current coupling. Observing current in the \hat{y} -direction (Figure 4.2(b)), above the central two tiles. Roughly halfway between the powered tiles and the unpowered electrode, the current changes direction ($y \sim 2\text{cm}$). This suggests that the coupled current is confined to a smaller region in front of the tiles (Will be shown more explicitly later). The current in the \hat{x} -direction (Figure 4.2(a)), again is strong in this region in front of the tile and decreases with distance from the powered tiles.

In the high current simulation there are some differences in the magnetic field (Figure 4.2(c)). Note that the scale of the magnetic field has gone from $2\mu\text{T}$ to $8\mu\text{T}$, a large increase in magnetic field strength. Again, there is a magnetic dipole between each tile-tile pair; the penetration depth of the dipole between tiles 3 and 4 is much smaller compared to the penetration depth in the 'low current' simulation. This is partially due to the decreased skin depth in

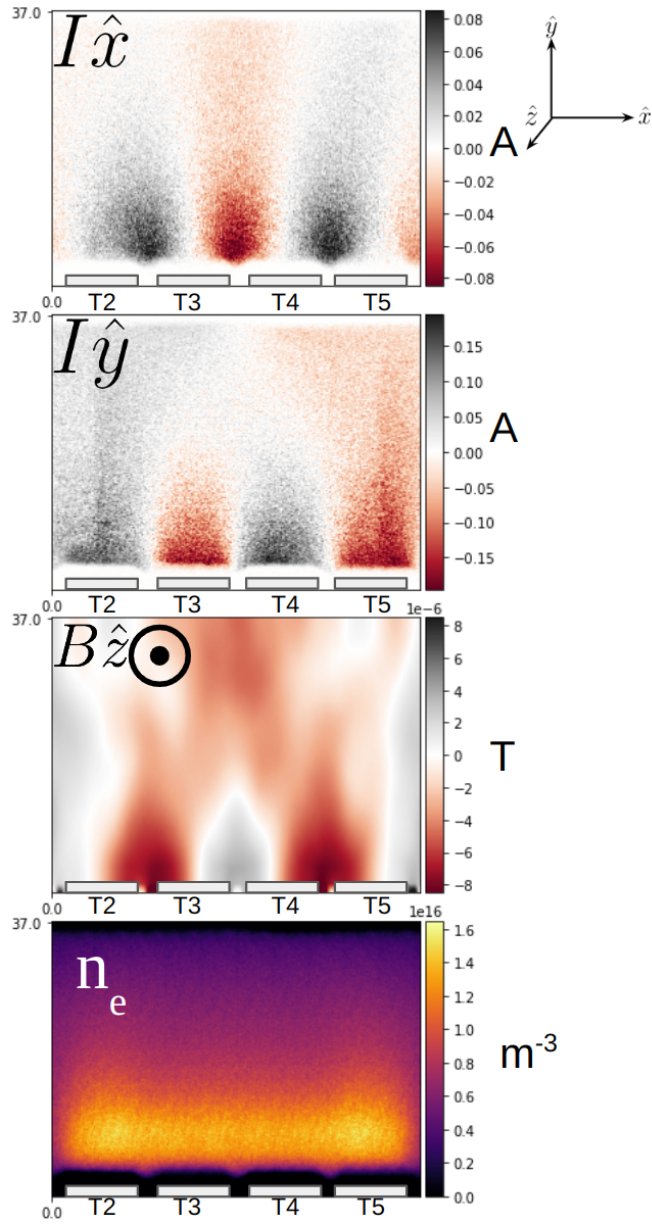


Figure 4.2: 2D profiles across the center 4 tiles for a simulation driven at 150A. Current in (a) x-direction, (b) y-direction, (c) Magnetic field in z-direction and (d) electron density. Currents and magnetic fields are defined as the total current or magnetic field in that particular cell.

the plasma. Moreover, in the higher current simulation, there is an increased coupled current, which more effectively shields out the magnetic field. Between the central tiles and the grounded electrode, a waveguide mode is observed in the magnetic field. The details of this are beyond the scope of this thesis, but it has some effect on the current path near the grounded electrode. Investigation of this phenomenon is subject to future work.

In the central tile-tile pair, the magnetic field is weaker than the magnetic field in the other two tile-tile pairs (tiles 2 and 3 and tiles 4 and 5). One reason for this is that the central two tiles are driving two tile-tile pairs (for example, tile 3 drives the coupled current between tiles 2 and 3 and the coupled current between tiles 3 and 4). Since tiles 2 and 5 are adjacent to an unpowered tile (*Tile₁* and *Tile₆*), they are only part of one tile-tile pair and are able to put more power into this tile-tile pair. This has also been observed experimentally [52]. Magnetic dipoles of equal strength can be obtained by driving the central two tiles with a larger driving current. In this thesis the central 4 tiles are driven with the same driving current. Since they are part of only one tile-tile pair, currents that move away from *Tile₂* and *Tile₅* towards the substrate are able to move across the whole plasma volume to the grounded electrode (seen in Figure 4.2(b)).

There are changes in the plasma density. Comparing Figures 4.1(d) and 4.2(d), note the scales of the density are different; A change from $7 \times 10^{15} m^{-3}$ to $16 \times 10^{15} m^{-3}$, where there is a change of drive current from 50A to 150A. There is a region of significantly higher plasma density situated close to the powered tiles, and we will call this region the 'coupling region', because most of the coupled current is confined to this region (this will be defined more rigorously further in the chapter). In Figure 4.2(d) this region is strongly peaked towards the powered tile and in figure 4.1(d) this region is more uniform vs y-position.

Moving from the coupling region toward the unpowered electrode, the plasma density is much lower. This region will be referred to as the 'non-coupling region', as most of the current in this region is not coupled current between adjacent tiles, becoming substrate current. The plasma density in front of $Tile_2$ and $Tile_5$ is higher, and the region of high plasma density extends further into the plasma in front of these tiles. Again this is due to coupling being stronger in the outer tile-tile pairs as discussed previously and has been observed experimentally [52].

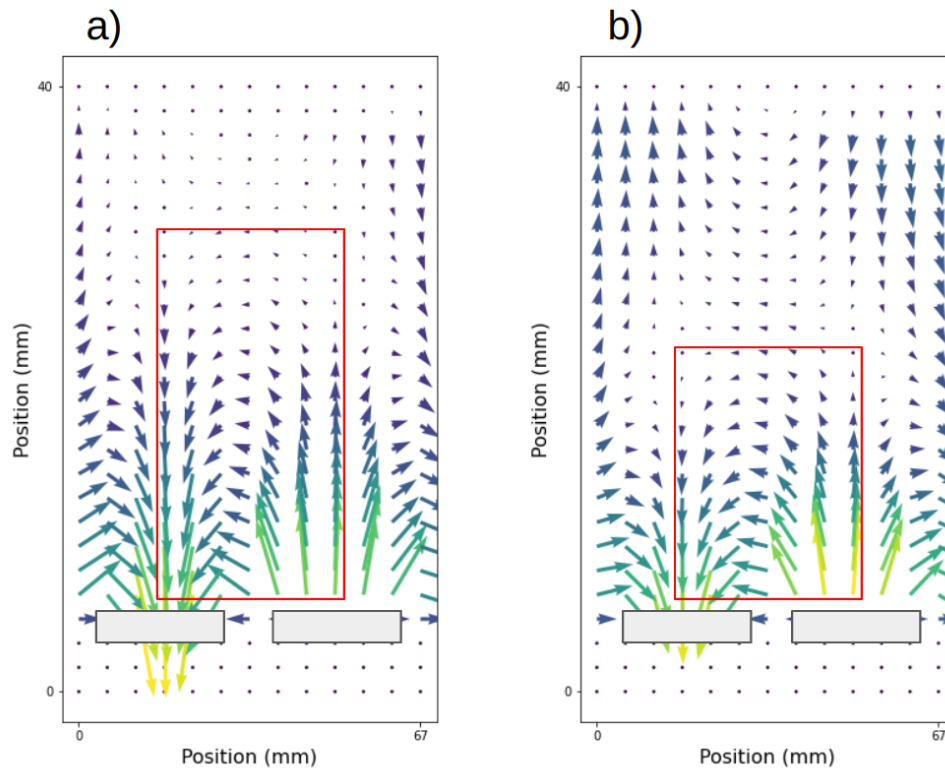


Figure 4.3: Conductive current vector in the plasma for lower current simulation (a), and higher current simulation (b).

Plasma currents in the plasma volume between the two central tiles and the grounded electrode for the low current simulation (a) and the higher current

simulation (b) are seen in Figure 4.3. This plot shows the location of current coupling in the plasma volume. The red box shows the approximate region where current is coupled. In the red box, the plasma current path is such that current moves away from one of the tiles, moves horizontally, parallel to tiles and towards the adjacent electrode. Outside of the red box, *rf* currents are much smaller and the current path points towards the grounded electrode.

In the 'low current' simulation (Figure 4.3(a)), the volume where current couples is large and takes up $\sim 70\%$ of the plasma volume. This region where current couples is defined as the coupling region. The reduction in size of the boundary of the coupling region is seen in Figure 4.3(b). Looking at the top boundary of the red box, the current vector below the boundary points (mostly) horizontally (in the $-\hat{x}$ -direction), with a small \hat{y} component pointing towards the tile. Following this current vector, the current points towards the tile. Just outside of the top boundary, the current vector also points (mostly) horizontally. However, following this current vector, the current points towards the grounded electrode, the \hat{y} component of this vector points towards the grounded electrode, and is 180 degrees out of phase from the current at the tile-face directly below. Inside of this boundary the 'coupled current' path is observed, and outside of it, the current points towards the grounded electrode. *rf* current density into the grounded electrode is comparatively quite small when compared to *rf* current density at the powered electrode.

In the 'high current' simulation (Figure 4.3(b)), the volume where current couples is comparatively smaller and extends roughly halfway across the plasma volume; Almost all of the 'coupled current' is confined to the coupling region, with small 'coupled current' outside of the coupling region. This shows that in a 'high current' simulation there is a decoupling in the two regions of the plasma.

4.3 Spatial density profile vs driving current

Figure 4.4 plots density as a function of y -position for all 7 tile-current conditions. The selected region spans from the center of the tile-tile gap between $Tile_1$ and $Tile_2$ to the center of the tile-tile gap between $Tile_5$ and $Tile_6$ in \hat{x} -direction, and across the whole plasma gap in the \hat{y} -direction. The density is averaged over the x -coordinate of this volume.

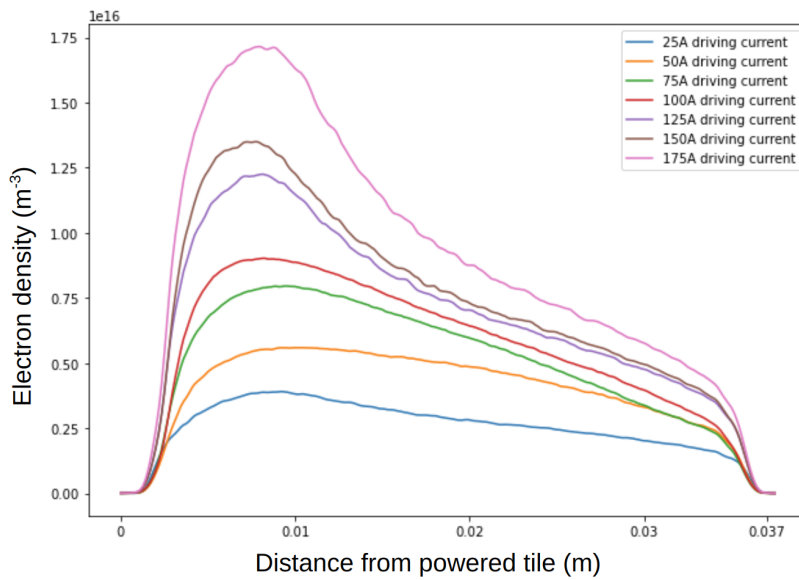


Figure 4.4: Plasma density in the \hat{y} -direction for all values of driving current.

Firstly, we observe curves at 50A, 75A and 100A. This contains the 'low current' simulations. In these simulations, the change in the plasma density across the plasma volume is rather gradual. The density profiles are as expected for a bounded plasma with ionization across the y -axis (That is concave down, with plasma diffusion towards the boundaries), but with preferential ionization towards the powered tile. For the 50A simulation (orange), the plasma density is roughly 30% larger at the peak in density ($y \approx 0.8\text{cm}$) than at $y = 2.5\text{cm}$ (roughly halfway towards the boundary). In the 100A simulation (red), the

plasma density roughly 60% larger. According to Maxwell-Boltzmann statistics, this change in density comes with plasma potential difference across the space the density difference is observed ($n_e(V) = n_0 \exp\left(\frac{e\Delta V}{k_B T_e}\right)$). The higher plasma density is attributed to the larger coupled current due to the horizontal electric fields (this is discussed further on in the chapter). The potential difference across the plasma from $y=0.8$ to $y=2.5$ is between 0.5V and 1.5V for these conditions.

In the 'high current' simulations (125A, 150A and 175A), the plasma density profile is quite different; There are distinct coupling and non-coupling regions. The density profile shows a sharp peak in the plasma density in the coupling region, followed by a concave-up into the non-coupling region. The change in plasma density between the peak (still $y\sim 0.8$) to $y=2.5$ is larger in this case; twice as large for 125A, and up to 2.7 as large at 175A. The potential difference across this distance is between 2V and 3V for these conditions. This change in density is consistent with the variation in plasma potential discussed in Section 3.3.3. There is a raised plasma potential in front of the powered electrodes, with some scale length into the plasma. The scale length is not known but the density profile as function of y -position provides some evidence of this plasma potential profile.

4.4 Difference between coupling and non-coupling region

In the coupling region and non-coupling regions of the plasma, there are certain differences in the behaviour of the plasma. The plasma density profile in three different regions of the plasma is shown in figure 4.5. This density was calculated in the plasma volume between the central 4 powered tiles and the grounded electrode. The red line shows the average plasma density in the coupling region (as defined in section 4.2, the size of the coupling region changes

for different values of drive current, where at lower drive current the coupling region extends further into the plasma, than at higher drive current), the blue line shows average plasma density in the non-coupling region (also defined in section 4.2, the size of this region also changes for different values of drive current), and the grey line shows the average plasma density in the plasma volume above the central 4 tiles.

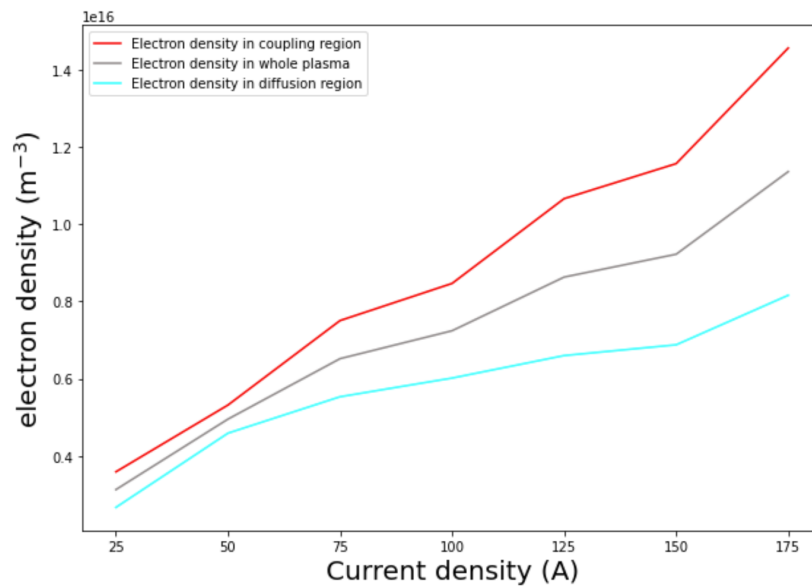


Figure 4.5: Plasma density in coupling region (red), non-coupling region (blue) and total plasma volume (grey)

The average plasma density in the coupling region (Figure 4.5 red line) increases linearly as a function of driving current. In the non-coupling region the average plasma density increases sublinearly. In the total plasma volume, the average plasma density lies somewhere between the two.

Shown in figure 4.6 is the spatial ionization profile vs y-position in the plasma volume between tiles 3 and 4 and the grounded electrode. A higher ionization rate is seen in front of the powered tiles. Moving away from the coupling region

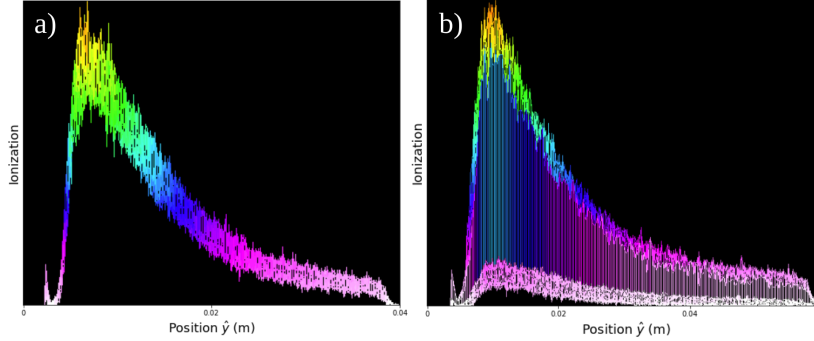


Figure 4.6: Ionization rate vs y-position, for (a) 50A driving current, (b) 150A driving current.

towards the grounded electrode ($y=4\text{cm}$), a decrease in the ionization rate is observed, with a much lower ionization rate in the non-coupling region. Note that figure 4.6(a) shows ionization for the 50A simulation, which is where the coupled current extends more than halfway into the plasma volume. In the simulation driven at 150A, the ionization profile remains largely the same but with even more ionization occurring in the high plasma density region near the powered tile.

To understand the localization of the ionization, the electron temperature is calculated in the plasma.

Electron velocity distribution was calculated (from the output of the PIC simulation) in the coupling region and non-coupling region between the central 4 tiles and grounded electrode with regions defined as in previous sections (Figure 4.7). The mean velocity of each distribution was found, and T_e was calculated from equation $v_{mean} = \sqrt{\frac{8k_b T}{\pi m_e}}$. The coupling region is observed to have a higher electron temperature than the non-coupling region for both simulations. The threshold for single step Argon ionization is a speed of $2.35 \times 10^6 \text{m/s}$. At 50A (Figure 4.7(a)) significantly larger portion of electrons in the coupling region

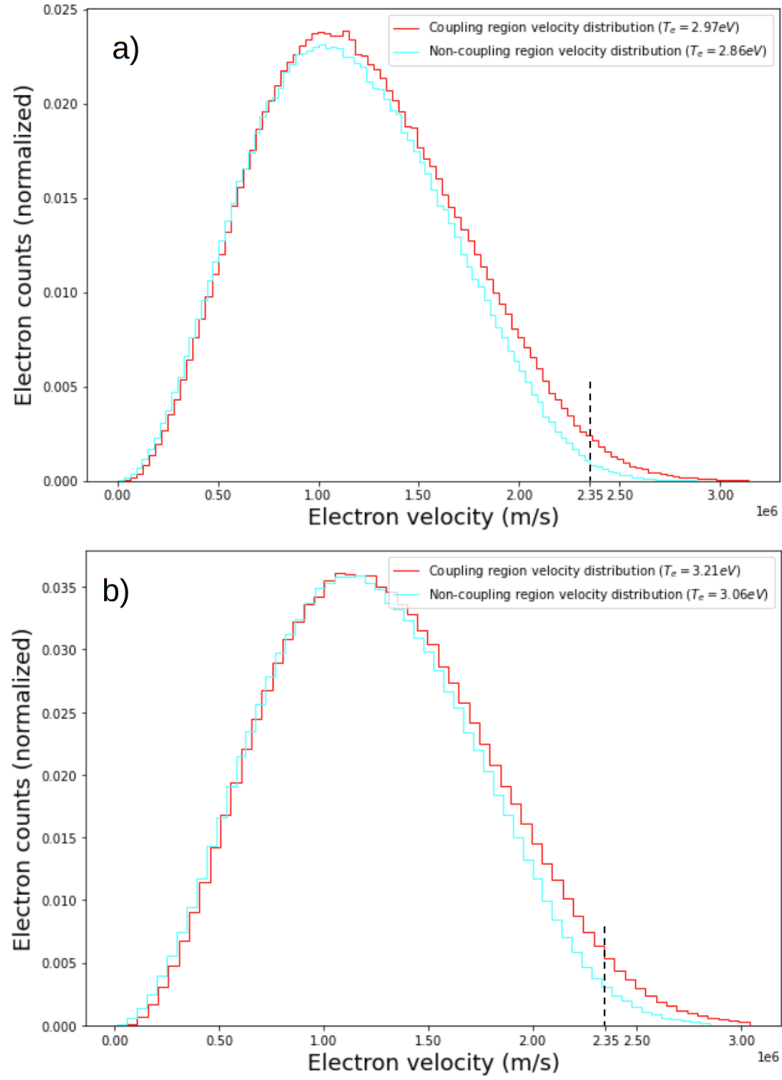


Figure 4.7: Velocity distribution in the coupling region (red), and non-coupling region (blue) for Simulation driven at 50A (a) and simulation driven at 150A (b). Threshold for single step Argon ionization in Xoopic is 15.76eV, equating to a velocity of 2.35×10^6 m/s shown on the x-axis.

are above this threshold than electrons in the non-coupling region. At 50A, a T_e of 2.97eV is observed in the coupling region with a T_e of 2.86eV in the non-coupling region. In the 150A simulation the T_e in the coupling region increases to 3.21eV, with T_e in the non-coupling region increasing to 3.06eV. In the coupling region there are significantly more electrons that can cause ionizing collisions than in the non-coupling region. Comparing the two simulations, more electrons have enough energy to cause ionization in the 150A simulation than in the 50A simulation.

The combination of the previous diagnostics shows that the plasma behaves differently in the coupling region and the non-coupling region. The coupling region has a higher density than the non-coupling region, which is sustained by a much higher ionization rate in this region. The higher electron temperature in the coupling region supports the higher ionization rate. The higher density in the coupling region doesn't spread to the non-coupling region due to the higher plasma potential, in the coupling region.

4.5 Voltage profile on differentially powered tiles

Tiles are current driven with a waveform of shape $I(t) = I_0 \sin(\omega t + \phi)$, resulting in a self-consistent voltage made of an *rf* oscillating component and a DC bias component. The time varying voltage between the back of the tile and grounded wall surrounding the simulation is shown in Figure 4.8(a). The resulting voltage is a sinusoidal wave with amplitude increasing linearly with driving current. The resulting voltage waveform lags the driving current by 90 degrees.

Figure 4.8(b) shows the amplitude of the voltage on the back of the tile. The capacitance between the back of the tile and ground is measured to be $C = 1.77nF$, resulting in a capacitive reactance $X_C = 0.56\Omega$. Applying Ohm's

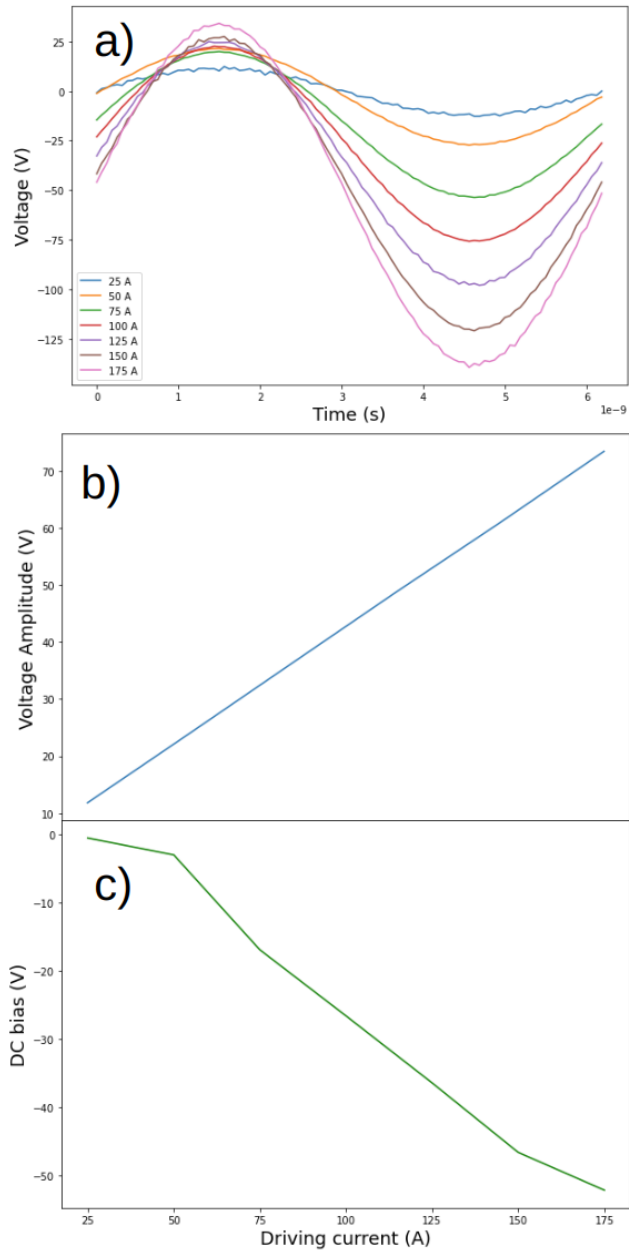


Figure 4.8: Tile voltage over and *rf* cycle (a), Amplitude of tile voltage(b), DC bias on tile (c)

law ($V = IZ$) shows that for every amp into the tile, a voltage of 0.56V can be driven between the tile and the wall. We observe a slope of 0.49V/A in figure 4.8(b), showing that every amp of current into the tile drives 0.49V between the tile and grounded wall. This means that only 12% of the current pushed into the tile is making it to the face of the tile and driving a voltage on the face of the tile, while 88% of the driving current is used to drive the voltage between the back of the tile and the ground surrounding the simulation.

The self consistent DC bias is plotted in Figure 4.8(c). For driving currents of 75A and greater, DC bias on the electrode changes linearly with driving frequency. At high values of driving current (over 75A) V_{rf} is over 35V. For a 3eV argon plasma, V_f is expected to be around 15eV. When V_{rf} is large in comparison to V_f , in order to reach a state where ion and electron flux are balanced over the *rf* cycle ($\langle \Gamma_i = \Gamma_e \rangle_{rf}$), the powered electrode must adopt a large DC bias.

When the driving current is lower (25A and 50A), V_{rf} is 12V and 24V respectively. This is not much larger than V_f , so the DC bias required in order to balance the electron and ion fluxes ($\langle \Gamma_i = \Gamma_e \rangle_{rf}$) must be small. This was investigated by Harvey et. al [1], where ion energies into the sheath were observed. Ions energies were dependent on the usual DC bias (which is established to preserve charge neutral flux), but also had a component due to the variation in plasma potential. The DC bias measured in our experiments are consistent with the measurements from Harvey et. al.

The powered tiles take on a large DC bias, and the voltage across the sheath of the powered tile is large when compared to the voltage across the sheath of the grounded tile. The plasma potential in the non-coupling region and the grounded electrode is between 15V and 20V for all values of driving current, which comes from the value of V_f along with a small *rf* current into the sheath

[1]. There are some *rfc* currents observed at the grounded electrode, which must be driven by a plasma potential that is higher than the 15V that is usually observed for a 3eV plasma. We don't know what the exact floating potential is, but we believe it to lie somewhere between 15 and 20V. This is similar to an asymmetric system where there is a small-area powered electrode, that adopts a high DC bias, and a large-area unpowered electrode to adopts a comparatively lower DC bias. In this differentially powered case, the tiles adopt a high DC bias without the need for a difference in electrode area.

Note that in some of the high current simulations, the peak tile voltage reaches values larger than the expected floating potential of 15-20V. In the simulation driven at 175A per tile, $V_{rf} = 87V$, and $V_{DC} = -53V$ the peak tile voltage reaches 34V. Remember, that there is a plasma potential variation in the region in front of the tiles (section 3.3.3). We expect that at this momentary peak, \tilde{V}_p at the tiles increases to a value close to this peak tile voltage. This is reflected by the electron density (Figure 4.4) which displays a peak near the powered electrode. At this high driving current condition, some momentary field reversal has been observed at this moment in time, where the tile voltage becomes larger than the plasma potential in front of the tile. This results in a period of rapid electron collection, to neutralize the charge balance. Details of this phenomenon are not fully understood, and are subject to future work.

4.6 Coupled current and substrate current scaling

Total coupled current is measured and total substrate current is measured in the plasma volume. These currents are calculated using the following method: A rectangular box is defined spanning from a single tile-face to the edge of the coupling region (in the \hat{y} -direction, shown in Figure 4.9), and from the centre of the tile-tile boundary on the left of that tile, to the centre of the tile-tile

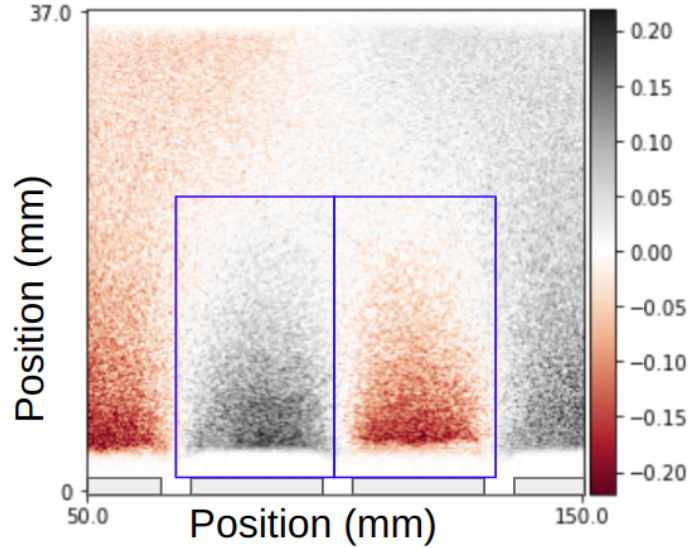


Figure 4.9: Plasma current in the \hat{y} -direction with two bounding boxes used to calculate total coupled current and total current into the substrate.

boundary on the right of that tile (in the \hat{x} -direction). Current in the \hat{x} -direction is measured through the vertical boundary of this box. This current in the \hat{x} -direction is the coupled current. For each tile, this current must be divided by two, as there are two tiles responsible for the coupled current between a tile-tile pair. The substrate current is defined as the current in the \hat{y} -direction, through the horizontal edge at the top of this box. Current moving through this region has passed through the coupling region and will reach the unpowered substrate.

In figure 4.10, coupled current and substrate current are shown as a function of driving current. Recall, from section 4.4.5, 88% of the driving current is used to drive an electric field between the tile and the wall, and only 12% of the driving current drives the plasma system. Coupled current is shown in Figure 4.10(a) and current towards the substrate is shown in Figure 4.10(b). Coupled current is much larger than substrate current; At low driving current, 76% of current moving away from the tile becomes coupled current, but at higher values

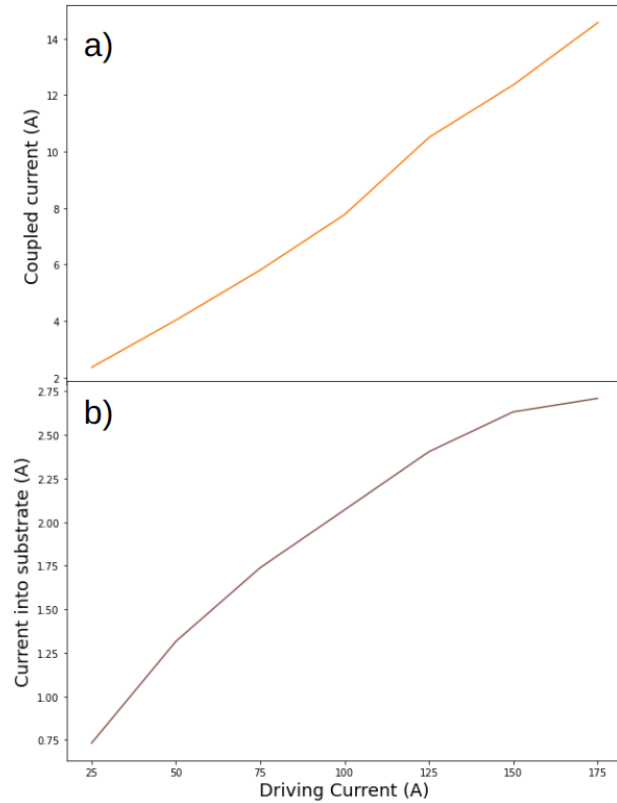


Figure 4.10: Coupled current (a), and current into the substrate (b) as a function of driving current.

of driving current, 84% becomes coupled current. This shows that as driving current increases, a larger fraction of current moving away from the powered tile becomes coupled current, and a smaller fraction becomes diffusion current. There is a superlinear relationship between coupled current and driving current, and a sublinear relationship between current into the substrate and driving current. This is clearly observed in Figure 4.11.

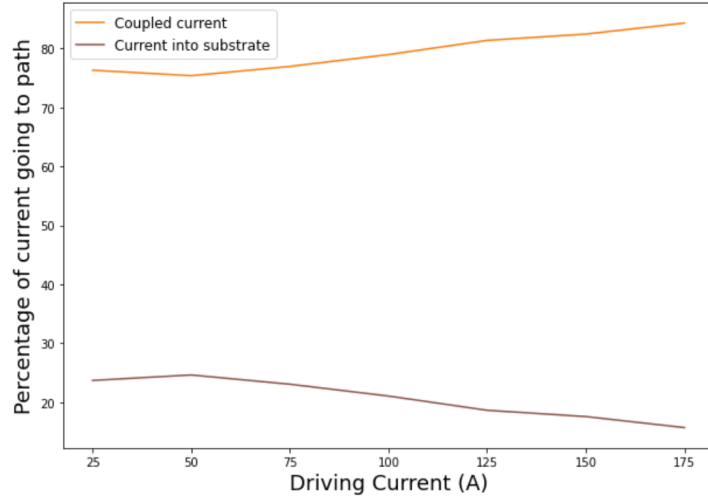


Figure 4.11: Fraction of total current turned into coupled current (orange), fraction of total current that moves towards the substrate (brown)

4.7 Electromagnetic response in the higher current simulation

In section 3.6.1 an analytical model of Generalized Ohm’s Law was applied to the Xoopic solution. In this low current case it was shown that this electrostatic approximation could reasonably describe the current in the plasma. In the high current case there are some noticeable differences in the current profile (seen in figure 4.12).

Observing currents in front of the two central tiles, in the analytical model, current decays exponentially vs y -position. In the current from the PIC simulation, there is a distinct sign change about halfway between the powered tiles and the grounded electrode. This shows that towards the grounded electrode the plasma may no longer obey the electrostatic approximation, and electromagnetic effects could be strong enough to create a significant impact on the plasma. Further investigation is subject to future work.

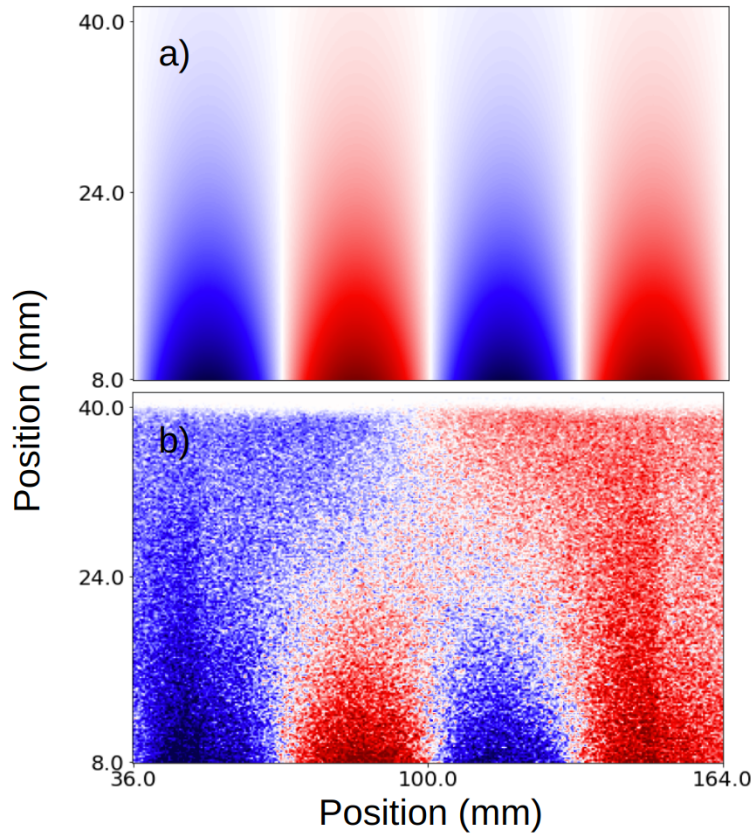


Figure 4.12: Current in the y -direction from the Generalized Ohm's Law model (a) compared to current in the y -direction from Xoopic

4.8 Summary

There are some differences in the plasma between the coupling region and non-coupling region. The coupling region has a higher plasma density, higher electron temperature, and a significantly higher ionization rate. Discussed in chapter 3, there is a spatio-temporal variation in the plasma potential in front of the tiles, driven by the tile voltage. The scale length of this voltage into the plasma is not known, but this voltage decreases as a function of distance from the tiles. The plasma potential in the \hat{y} -direction must follow this voltage pro-

file. This potential causes the plasma to have a higher plasma density at the tiles than in the non-coupling region (observed in figure 4.4). The density profile in y-direction provides some evidence for the scale length and shape of the voltage. The higher electron temperature in the coupling region drives a higher ionization rate. This is observed for all values of driving current, but most prominent in the higher current regions (At 175A of driving current, the plasma density in the coupling region is up to 2.7 times as large as the plasma density in the non-coupling region). There is some diffusion from the coupling region to the non-coupling region and the grounded electrode, but the higher plasma potential at the tile is able to sustain this difference in plasma density.

As driving current increases, a larger fraction of current in the plasma becomes driving current rather than coupled current, 84% of driving current becomes coupled current in the 175A simulation. A potential reason for this can be described by observing the tile voltage. As driving current increases, tile voltage becomes greater. At high values of drive current the DC bias on tile scales with the driving current. At high values of driving current, the maximum value of tile voltage over the *rf* cycle increases. The higher the tile voltage, the smaller the potential that the electrons have to overcome to strike the tile. At higher drive current, more electrons strike the tile during the period of electron collection. At this moment in time, plasma potential in front of the tile increases more meaning that there is a larger electrostatic electric field parallel to the face of the tiles. This results in a larger coupled current. Moreover, at high drive currents, the increased plasma density means that the plasma is more conductive, and a greater current can be driven by the horizontal electric field.

5 Conclusion

A multi-tile differentially powered VHF CCP has been investigated using a PIC simulation code called Xoopic [2]. In chapter 3, the physics of this plasma system was investigated. A "coupled current" was identified which 'couples' electron current in the plasma that is moving away from one tile, with current that is moving towards the adjacent tile. A smaller amount of current moves across the plasma volume where it reaches the substrate (substrate current). Two physical phenomena are described that are responsible for driving the 'coupled current'.

The first is an electromagnetic phenomenon that drives this coupled current is described; *rf* currents travelling on the surface of the tiles create a magnetic dipole between adjacent tiles. This magnetic dipole creates an induced electric field that drives current parallel to the face of the tiles. This magnetic field and electric field is observed in Xoopic[2] simulations.

The second is an electrostatic phenomenon; An *rf* oscillation in the plasma potential creates an electric field parallel to the face of the tiles. While the tile voltage reaches a maximum over the *rf* cycle, the plasma potential in front of that tile increases for that moment in the *rf* cycle. This plasma potential oscillation extends into the pre-sheath region of the plasma. Since the tiles are differentially powered, voltage on adjacent tiles is at a 180 degrees out of phase. This results in a variation in the plasma potential. This variation in the plasma potential creates an electric field which drives a current parallel to the face of the tiles. Higher harmonics of the driving frequency are observed in the electric field that drives the coupled current (horizontal electric field). This is attributed to the electrostatic phenomenon.

A Generalized Ohm's Law model was developed to separate the electro-

static and electromagnetic phenomena. This model is a simpler electrostatic approximation of our plasma system, neglecting displacement current. It was found that this model was an excellent fit to the plasma system, with 5% difference in fit. An analytical model of Generalized Ohm's Law was created, and resultant current densities accurately fitted the profile of the currents from Xoopic. This indicates that the electrostatic approximation may be a good description of the plasma. To further determine which phenomenon was driving the coupled current, Faraday's Law was solved in the plasma volume above the central tile-tile pair in the 75A driving current simulation. Solving Faraday's Law determines whether the magnetic field creates an induced electric field of comparable strength to the electric fields measured in the simulation. The induced electric field is a factor of 20 smaller than the measured electric field. It is determined that in the 75A driving current system, the electric field is driven by the electrostatic phenomenon with minimal influence from the electromagnetic phenomenon.

In chapter 4 changes in behaviour of the plasma are observed by changing the magnitude of the drive current. Two different regions in the plasma are identified; A coupling region and a non-coupling region. In the coupling region *rf* currents couple between adjacent tiles. In the non-coupling region *rf* currents are move into the grounded electrode. The plasma is observed to behave differently in these two regions; In the coupling region the plasma has higher density, higher electron temperature and a much higher ionization rate than in the non-coupling region. The combination of increased plasma density, higher electron temperature and high *rf* currents in the coupling region are self-consistent and indicative of a new *rf* power coupling regime in the multi-tile plasma source. The large current differences between face of tile and substrate current are indicative

of an asymmetric CCP. Power deposited by the coupled currents are additional to the standard high frequency CCP electron heating.

As driving current is increased, a larger fraction of the current becomes "coupled current" rather than "substrate current". At the lowest value of driving current 76% of current becomes coupled current, and at the highest value driving current 84% of driving current becomes coupled current.

6 Appendix

Plasma system and operational parameters

Outer tiles unpowered

The two outer tiles are left unpowered. It was observed that near-field effects can occur between the tile-corner and the ground surface, which can result in significant transients while the simulation is settling into the steady-state solution. For some conditions this results in an extended sheath above $Tile_1$ and $Tile_6$, grossly affecting the plasma over the central tiles. Much of these instabilities are the result of 'ideal-material-properties' associated with the PIC simulation, and would not be realized in an experimental system with charge-bleeding through the substrate, and along dielectric surfaces.

Current injection and Tile voltage

Figure 6.1 is a detailed schematic of how a single tile functions in the Xoopic simulation. With reference to this figure, we will describe how current is injected into the tile, and how the tile voltage is calculated.

Current is injected into the back of the tile using a Xoopic [2] current region as shown in figure 6.1. The current region delivers a predetermined amount of current in a given direction. In the presented simulation, the current region is 3 cells wide, and each cell delivers 25A into the $+\hat{y}$ -direction (into the high-K dielectric), meaning that a total of 75A is injected into the tile. Between the tile and the current region, a very high-K dielectric is placed (relative dielectric of 10000, so that the impedance remains small), and serves the function of a blocking capacitor.

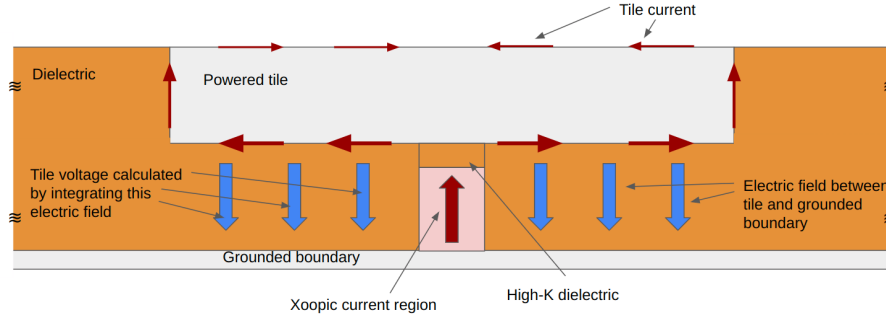


Figure 6.1: A single powered tile in the 2D array of differentially powered tiles, Showing method of current injection into the tile via a Xoopic "current region". Self-consistent electric field between the tile and grounded boundary is shown, and is used to calculate the time-varying *rf* voltage on the powered tile.

Tile voltage, V_{Tile} is calculated through measuring electric field between the tile and the grounded boundary. This electric field is a self-consistent output of the simulation; no functional dependence has been imposed on this electric field. Through the simple equation of $V = E \cdot m$, the potential difference between the grounded boundary and the tile can be calculated. The resultant V_{Tile} can be observed in black in figure 3.7(a). The result is that V_{Tile} is a sinusoidal waveform, lagging the driving current by 90 degrees, with a DC bias of -17V and an amplitude of 37V. The DC bias is a self-consistent result of the simulation, as no DC bias has been asserted on the driving current.

When using an electromagnetic solver, there can be spatial variation in voltage on the tile. In this simulation, the wavelength of the driving frequency is sufficiently long (1.88m in vacuum) and the tiles are sufficiently small (25mm x 1.25mm) such that no spatial variation in V_{Tile} is measured. The capacitance between the back of the tile and the surrounding ground is large enough that ion current through the sheath into the tile does not change the voltage on the tile by a significant amount over the *rf* cycle, resulting in a V_{Tile} that

has a stable *rf* amplitude and a DC bias component that does not change over many *rf* cycles. The capacitance between the back of the tile is 1.77nF, giving an impedance of 0.56Ω . With a driving current of 75A, and a self-consistent *rf* voltage of 37V, this means that 88% of the current into the tile is being used to drive the voltage between the tile and the grounded wall. Only 9A of current into the back of the tile makes it to the front of the tile, delivering power to the plasma. This adds stability to the computation as changes in plasma behaviour result in only small changes in the electromagnetic solution.

Operational parameters of simulation

In Xoopic, a grid of 512 cells in the \hat{x} -direction and 256 cells in the \hat{y} -direction is used, resulting in a cell size of (.391mm x .156mm). A timestep of 2.5×10^{-13} s is used. These input parameters satisfy the CFL stability condition that a photon can't travel more than one cell length in a single timestep ($c\Delta t < \Delta x$), and the condition that a single Debye length is a close to the length one cell length (In this case the Debye length is roughly equal to the cell size in the \hat{y} -direction) [21]. A sinusoidal current with amplitude 75A, with frequency of 160MHz is pushed into each of the powered tiles. For the simulation, the tiles are all driven independently, but in figure 3.2 there is an AC source which shows how the tiles would be driven as a push-pull pair, analogous to the experimental implementation.

The simulation is run on a multi-threaded version of Xoopic, and is run on 16 threads. Multi-threading is achieved by splitting the simulation into 16 vertical slices, each being simulated on a separate thread.

A table of operational parameters is displayed below.

Operational parameter	Value of parameter
x-grid	512 cells, 0.391 mm per cell
y-grid	256 cells, 0.156 mm per cell (finer for sheath resolution, $\lambda_D = 0.165$ mm)
Gas	argon 50mTorr
timestep	2.5×10^{-13} s
Tile size	25mm \hat{x} , 1.25mm \hat{y}
Tile-tile gap	7mm
Driving current, I_0	75A into the back of 1m deep tile
Driving frequency, f	$f = 160$ MHz
Driving function	$I(t) = I_0 \cos(\frac{f}{2\pi}t)$
Secondary electron coefficient	0.1
Capacitance between back of tile by backside dielectric	1.77nF

Power coupling

Functional dependence of electromagnetic field

The magnetic field is a self-consistent result of the simulation. The induced magnetic field is sinusoidal. Applying Faraday's law it is clear that the magnitude of the induced electric field scales with driving frequency, and lags the magnetic field by 90 degrees.

$$B(t) = B_0 \sin(\omega t + \phi) \quad (6.1)$$

$$\oint E \cdot dl = -\frac{\partial B}{\partial t} \quad (6.2)$$

$$\oint E \cdot dl = -\omega B_0 \cos(\omega t + \phi) \quad (6.3)$$

Combining Eqn 6.1 and Eqn 6.2 The induced *rfelectric* field scales with ω_{rf} and lags the current into the tile by 90 degrees.

Striping between core boundaries

All Xoopic simulations were multi-threaded, most run on 16 individual threads. Many of the plots were made by restarting the simulation on fewer threads or dumping all threads and recombining individual diagnostics. Striping is seen dominantly in the argon and electron density. It was unclear if the electron density stripes at the boundaries were faults in the code reporting, or even in the validity of the code. To test this simulations run on 16 threads were restarted on fewer threads (8 or 4) to see if the striping would disappear. If the stripes in the electron density were real features of the electron profile used within the simulation (and not just a reporting error) then the electron profile would relax to a "smooth" profile when restarted with fewer threads (and larger plasma volumes per thread). This did not occur, suggesting that the stripes do not affect the actual electron and ion densities. Moreover, Current pathes, magnetic fields, and electric fields display the same behaviour in simulations with striping and in simulations without striping.

References

- [1] Harvey C, Sirse N, Gaman C, Ellingboe AR. Mode transition in an oxygen low-pressure, very high frequency (162 MHz), multi-tile electrode capacitively coupled plasma. *Physics of Plasmas*. 2020 Nov;27(11):110701.
- [2] Verboncoeur JP, Langdon AB, Gladd NT. An object-oriented electromagnetic PIC code. *Computer Physics Communications*. 1995 May;87(1-2):199–211.
- [3] Hershkowitz N, Cho MH, Pruski J. Mechanical variation of plasma potential, electron temperature and plasma density. *Plasma Sources Science and Technology*. 1992;1(2):87–93.
- [4] Brault P, Thomann AL, Cavarroc M. Theory and molecular simulations of plasma sputtering, transport and deposition processes. *The European Physical Journal D*. 2023 Feb;77(2).
- [5] Randhawa H. Review of plasma-assisted deposition processes. *Thin Solid Films*. 1991 Feb;196(2):329–349.
- [6] Lafleur T, Booth JP. Control of the ion flux and ion energy in CCP discharges using non-sinusoidal voltage waveforms. *Journal of Physics D: Applied Physics*. 2012 Sep;45(39):395203.
- [7] Lee JK, Manuilenko OV, Babaeva NY, Kim HC, Shon JW. Ion energy distribution control in single and dual frequency capacitive plasma sources. *Plasma Sources Science and Technology*. 2005 Jan;14(1):89–97.
- [8] Sharma S, Sirse N, Turner MM, Ellingboe AR. Influence of excitation frequency on the metastable atoms and electron energy distribution function in a capacitively coupled argon discharge. *Physics of Plasmas*. 2018 Jun;25(6):063501.

- [9] Korolov I, Donkó Z, Czarnetzki U, Schulze J. The effect of the driving frequencies on the electrical asymmetry of dual-frequency capacitively coupled plasmas. *Journal of Physics D: Applied Physics*. 2012 Oct;45(46):465205.
- [10] Sharma S, Sen A, Sirse N, Turner MM, Ellingboe AR. Plasma density and ion energy control via driving frequency and applied voltage in a collisionless capacitively coupled plasma discharge. *Physics of Plasmas*. 2018 Aug;25(8):080705.
- [11] Vahedi V, Birdsall CK, Lieberman MA, DiPeso G, Rognlien TD. Verification of frequency scaling laws for capacitive radio-frequency discharges using two-dimensional simulations. *Physics of Fluids B: Plasma Physics*. 1993;5(7):2719–2729.
- [12] Finger F, Hapke P, Luysberg M, Carius R, Wagner H, Scheib M. Improvement of grain size and deposition rate of microcrystalline silicon by use of very high frequency glow discharge. *Applied Physics Letters*. 1994 Nov;65(20):2588–2590.
- [13] Sirse N, Harvey C, Gaman C, Ellingboe AR. Investigation of plasma uniformity, rotational and vibrational temperature in a 162 mhz multi-electrode capacitive discharge. *Journal of Physics D: Applied Physics*. 2020;53(33):335203.
- [14] Ryan K, O’Farrell D, Ellingboe AR. Spatial structure of plasma potential oscillation and ion saturation current in VHF multi-tile electrode plasma source. *Current Applied Physics*. 2011 Sep;11(5):S114–S116.
- [15] Kallio E, Chaufray JY, Modolo R, Snowden D, Winglee R. Modeling of Venus, Mars, and Titan. *Space Science Reviews*. 2011 Oct;162(1-4):267–307.

- [16] Harned DS. Quasineutral hybrid simulation of macroscopic plasma phenomena. *Journal of Computational Physics*. 1982 Sep;47(3):452–462.
- [17] Meierbachtol CS, Greenwood AD, Verboncoeur JP, Shanker B. Conformal Electromagnetic Particle in Cell: A Review. *IEEE Transactions on Plasma Science*. 2015 Nov;43(11):3778–3793.
- [18] Chevalier M, Luebbers RJ, Cable V. FDTD local grid with material traverse. *IEEE Transactions on Antennas and Propagation*. 1997 Mar;45(3):411–421.
- [19] Rambo PW. Numerical Heating in Hybrid Plasma Simulations. *Journal of Computational Physics*. 1997 May;133(1):173–180.
- [20] Vass M, Palla P, Hartmann PE. Revisiting the numerical stability/accuracy conditions of explicit PIC/MCC simulations of low-temperature gas discharges. *Plasma Sources Science and Technology*. 2022 May;31(6):064001–064001.
- [21] Barnes DC, Chacón L. Finite spatial-grid effects in energy-conserving particle-in-cell algorithms. *Computer Physics Communications*. 2021;258:107560.
- [22] Birdsall CK, Langdon AR. *Plasma Physics via Computer Simulation*. Institute of Physics; 1991.
- [23] *Plasma applications for material modification: from microelectronics to biological materials*. Singapore: Jenny Stanford Publishing; 2022.
- [24] Marchack N, Buzi L, Farmer DB, Miyazoe H, Papalia JM, Yan H, et al. Plasma processing for advanced microelectronics beyond CMOS. *Journal of Applied Physics*. 2021 Aug;130(8):080901. Available from: <https://aip.scitation.org/doi/10.1063/5.0053666>.

- [25] Makabe T, Petrovic ZL. Plasma Electronics. 1st ed. Taylor & Francis; 2006.
- [26] Rossnagel SM, Sherman A, Turner F. Plasma-enhanced atomic layer deposition of Ta and Ti for interconnect diffusion barriers. *Journal of Vacuum Science Technology B: Microelectronics and Nanometer Structures Processing, Measurement, and Phenomena*. 2000 Jul;18(4):2016–2020. Available from: <https://avs.scitation.org/doi/abs/10.1116/1.1305809>.
- [27] Iwase T, Kamaji Y, Kang SY, Koga K, Kuboi N, Nakamura M, et al. Progress and perspectives in dry processes for nanoscale feature fabrication: fine pattern transfer and high-aspect-ratio feature formation. *Japanese Journal of Applied Physics*. 2019 May;58(SE):SE0802.
- [28] Manova D, Gerlach JW, Mändl S. Thin Film Deposition Using Energetic Ions. *Materials*. 2010 Jul;3(8):4109–4141.
- [29] Schwarzenbach W, Howling AA, Fivaz M, Brunner S, Hollenstein C. Sheath impedance effects in very high frequency plasma experiments. *Journal of Vacuum Science & Technology A: Vacuum, Surfaces, and Films*. 1996;14(1):132–138.
- [30] Chabert P, Braithwaite N. Physics of Radio-Frequency Plasmas. 1st ed. Cambridge University Press; 2011. Available from: <https://www.cambridge.org/core/product/identifier/9780511974342/type/book>.
- [31] Oehrlein GS. Dry etching damage of silicon: A review. *Materials Science and Engineering: B*. 1989 Oct;4(1–4):441–450. Available from: <https://linkinghub.elsevier.com/retrieve/pii/0921510789902845>.
- [32] T Carver C, J Plombon J, E Romero P, Suri S, A Tronic T, B Turkot R. Atomic Layer Etching: An Industry Perspective. *ECS Journal of Solid*

- State Science and Technology. 2015;4(6):N5005–N5009. Available from: <https://iopscience.iop.org/article/10.1149/2.0021506jss>.
- [33] Ohba T, Yang W, Tan S, Kanarik KJ, Nojiri K. Atomic layer etching of GaN and AlGaN using directional plasma-enhanced approach. *Plasma Sources Science and Technology*. 2017 May;56(6S2):06HB06–06HB06.
- [34] Perret A, Chabert P, Booth JP, Jolly J, Guillon J, Auvray P. Ion flux nonuniformities in large-area high-frequency capacitive discharges. *Applied Physics Letters*. 2003 Jul;83(2):243–245.
- [35] Liu YX, Zhang YR, Bogaerts A, Wang YN. Electromagnetic effects in high-frequency large-area capacitive discharges: A review. *Journal of Vacuum Science & Technology A: Vacuum, Surfaces, and Films*. 2015 Mar;33(2):020801.
- [36] Perrin J, Schmitt J, Hollenstein C, Howling A, Sansonnens L. The physics of plasma-enhanced chemical vapour deposition for large-area coating: Industrial application to flat panel displays and solar cells. *Plasma Physics and Controlled Fusion*. 2000;42(12B).
- [37] Colgan MJ, Meyyappan M, Murnick DE. Very high-frequency capacitively coupled argon discharges. *Plasma Sources Science and Technology*. 1994 May;3(2):181–189. Available from: <https://iopscience.iop.org/article/10.1088/0963-0252/3/2/009>.
- [38] Barnat EV, Miller PA, Hebner GA, Paterson AM, Panagopoulos T, Hammond E, et al. Measured radial dependence of the peak sheath voltages present in very high frequency capacitive discharges. *Applied Physics Letters*. 2007 May;90(20):201503.

- [39] Abdel-Fattah E, Sugai H. Combined effects of gas pressure and exciting frequency on electron energy distribution functions in hydrogen capacitively coupled plasmas. *Physics of Plasmas*. 2013 Feb;20(2):023501.
- [40] Sharma S, Sirse N, Kaw PK, Turner MM, Ellingboe AR. Effect of driving frequency on the electron energy distribution function and electron-sheath interaction in a low pressure capacitively coupled plasma. *Physics of Plasmas*. 2016 Nov;23(11):110701.
- [41] Oh IK, Yoo G, Yoon CM, Kim TH, Yeom GY, Kim K, et al. Very high frequency plasma reactant for atomic layer deposition. *Applied Surface Science*. 2016;387:109–117.
- [42] Curtins H, Wyrsh N, Favre M, Shah AV. Influence of plasma excitation frequency for a-Si:H thin film deposition. *Plasma Chemistry and Plasma Processing*. 1987 Sep;7(3):267–273. Available from: <https://doi.org/10.1007/BF01016517>.
- [43] Lieberman MA, Booth JP, Chabert P, Rax JM, Turner MM. Standing wave and skin effects in large-area, high-frequency capacitive discharges. *Plasma Sources Science and Technology*. 2002 Jun;11(3):283–293.
- [44] Ellingboe AR. Plasma source; U.S. Patent US7342361B2, Mar. 2008.
- [45] Michna T, Ellingboe AR. Characterisation of an RF power splitter for multi-tile PECVD systems application. *Current Applied Physics*. 2011 Sep;11(5):S9–S11.
- [46] Monaghan E, Yeom GY, Ellingboe AR. Measurement of NC-si:H film uniformity and diagnosis of plasma spatial structure produced by a very high frequency, differentially powered, multi-tile plasma source. *Vacuum*. 2015;119:34–46.

- [47] Ryan K. Spatial diagnostics of plasma produced by a VHF multi-tile electrode. School of Physical Sciences, Dublin City University; 2012. Available from: <https://doras.dcu.ie/17495/1/120512KRThesis.pdf>.
- [48] Mohr S, Schüngel E, Schulze J, Czarnetzki U. Field reversals in electrically asymmetric capacitively coupled radio-frequency discharges in hydrogen. *Journal of Physics D: Applied Physics*. 2013 Oct;46(43):435201.
- [49] Czarnetzki U, Luggenhölscher D, Döbele HF. Space and time resolved electric field measurements in helium and hydrogen RF-discharges. *Plasma Sources Science and Technology*. 1999 May;8(2):230–248.
- [50] Martin M. Generalized Ohm’s Law at the Plasma-Vacuum Interface [PhD Thesis]. Cornell University; 2010.
- [51] Raju GG. Electron-atom collision cross sections in argon: an analysis and comments. *IEEE Transactions on Dielectrics and Electrical Insulation*. 2004 Aug;11(4):649–673.
- [52] O’Farell D. Improving plasma density uniformities at VHF/UHF operating frequencies using a scalable, multi-electrode, VHF/UHF plasma source; 2011.